Solid Oxide Fuel Cell Hybrid System for Distributed Power Generation

Phase 1 Topical Report

July 2001 to June 2004

Nguyen Minh

September 2004

Performed under DOE/NETL Cooperative Agreement

DE-FC26-01NT40779

GE Hybrid Power Generation Systems

19310 Pacific Gateway Drive

Torrance, CA 90502

Disclaimer

Abstract

This report summarizes the work performed by Hybrid Power Generation Systems, LLC (HPGS) in Phase 1 System Design and Technical Barrier Resolution tasks under Cooperative Agreement DE-FC26-01NT40779 for the U. S. Department of Energy, National Energy Technology Laboratory (DOE/NETL) entitled “Solid Oxide Fuel Cell Hybrid System for Distributed Power Generation”. The main objective of this project is to develop and demonstrate the feasibility of a highly efficient hybrid system integrating a planar Solid Oxide Fuel Cell (SOFC) and a micro-turbine.

A conceptual hybrid system design was selected for analysis and evaluation. The selected system is estimated to have over 65% system efficiency, a first cost of approximately $650/kW, and a cost of electricity of 8.4 cents/kW-hr. A control strategy and conceptual control design have been developed for the system.

A number of SOFC module tests have been completed to evaluate the pressure impact to performance stability. The results show that the operating pressure accelerates the performance degradation.

Several experiments were conducted to explore the effects of pressure on carbon formation. While carbon formation is favored at pressurized conditions, the conditions at which carbon formation occurs in a functioning cell is difficult to predict. Experimental observations on a functioning cell have verified that carbon deposition does not occur in the cell at steam-to-carbon ratios lower than the steady-state design point for hybrid systems.

Heat exchanger design, fabrication and performance testing as well as oxidation testing to support heat exchanger life analysis were also conducted. Performance tests of the prototype heat exchanger yielded heat transfer and pressure drop characteristics consistent with the heat exchanger specification.

Table of Contents

List of Figures

List of Tables

Executive Summary

This report presents the work leading to the conceptual design of the full-scale hybrid system, incorporating a Honeywell Parallon 75 microturbine and planar solid oxide fuel cell (SOFC). The system design with anode and cathode recycle was downselected. This system concept is estimated to have over 65% efficiency and the highest reliability and availability compared to the other four system concepts evaluated. The down selected system is estimated to have a first cost of $646/kW and a cost of electricity of 8.4 cents/kW-hour. Part-load analysis of this system showed that the efficiency of the system remains over 60% down to power levels of 200 kW. Several trade studies were completed for the control of this system. These trades helped develop an understanding of the controllability of the system and investigate strategies for controlling the proposed system.

This report also summarizes the results from the phase 1 SOFC barrier resolution task. In particular, the experimental work related to the impact of pressure on cell performance degradation and the carbon formation boundary and the results from the high temperature heat exchanger barrier resolution task.

A number of SOFC module tests have been completed to evaluate the pressure impact to performance stability. The results show that the operating pressure accelerates the performance degradation. The potential causes of the performance decay include oxidation of the metal interconnect, chromium poisoning to electrodes, interface resistance increase, electrode microstructure changes, back diffusion/leakage, and/or electrode conditioning process. The dominant degradation mechanisms remain unclear. Both interconnect oxidation and Cr transport to cathode were evident based in post-test analysis.

Several experiments were conducted to explore the effects of pressure on carbon formation. While carbon formation is favored at pressurized conditions, the conditions at which carbon formation occurs in a functioning cell is difficult to predict. Experimental observations on a functioning cell have verified that carbon deposition does not occur in the cell at steam-to-carbon ratios lower than the steady-state design point for hybrid systems. These results are in good agreement with theoretical analysis. These experiments were conducted on 3-inch and 4 3/8-inch SOFC cells operating at 4 atmospheres.

The high temperature heat exchanger barrier resolution task included heat exchanger design, fabrication, and performance testing, as well as oxidation testing to support the heat exchanger life analysis. Performance tests of the prototype heat exchanger yielded heat transfer and pressure drop characteristics consistent with the heat exchanger specification. Coupon testing on Inconel 625 and Haynes 230 samples completed over 3000 hours of exposure to SOFC conditions. A correlation of the oxide layer thickness as a function of time has been determined from the coupon sample data at three temperatures.

Experimental

All experimental work currently performed on the program is contained in task 1A.2, Barrier Resolution. Experimental methods employed in this task is described and discussed in sections 2.1.4 and 2.2.1.1.

Results and Discussion

1 SYSTEM DESIGN

1.1 Conceptual System Design

Four different system configurations were considered in the trade study from which one configuration is down selected for further analysis and optimization. The down-selection to one system concept is based on system efficiency, reliability, cost, and the cost of electricity (COE). COE provides a means to trade system efficiency against reliability and cost.

The approach undertaken in the trade study consists of the following steps:

(1) The efficiency of all system concepts is analyzed as functions of system parameters;

(2) A local maximum of the resulting system efficiency function is determined for each system concept;

(3) System components are identified for each candidate system concept (some components may be common across the candidate systems);

(4) System cost and reliability are estimated;

(5) COE models are created and system COE is estimated;

(6) The system design point is adjusted if necessary to improve system COE at the acceptable expense of system efficiency;

(7) Steps (1) through (6) are repeated until an optimized system design is found for each candidate;

(8) The system with the “best” optimized solution is down selected.

System performance (efficiency), reliability, first cost, and COE analysis are described in the following sections.

1.1.1 Performance Analysis

A steady state system performance model is the basis for estimating system power and efficiency for a set of component performance assumptions. The components are modeled in a sequential modular fashion using the ASPEN PLUS steady state platform and its thermodynamic database. The model has been optimized for speed, thus enabling efficient system optimization using a large number of model runs.

The system is optimized at the peak power of the Parallon 75 microturbine, corresponding to its peak speed, while the SOFC design and operating points are varied. Thus, the air flow and pressure is fixed, but the SOFC cell operating voltage, fuel utilization, and total electrical power output is varied to maximize system efficiency while maintaining all design constraints of the system.

In general, efficiency increases as the ratio of the power output from the SOFC stack to that of the turbine increases. This is because the fuel cell is more efficient than the turbine. Thus, at this peak condition there is no firing of fresh fuel to increase the turbine inlet temperature. The stack exhaust temperature and the fuel utilization determine the turbine inlet temperature. However, in order to achieve high component reliability, the turbine inlet temperature is restricted. Similarly, temperature limitations are set for the burners, the recuperators, the high temperature air preheaters, and the stack.

The sensitivity of cell voltage (at 80% fuel utilization) and stack fuel utilization (at cell voltage of 0.75V) on systems efficiency and net system power output is shown in Figure 1 for concept 1. The resulting net power output for concept 1 is in the range of 500 to 900 kW depending on the cell voltage and fuel utilization. The net power output increases as the cell voltage or the fuel utilization increases. This is because the efficiency of the stack increases as the cell voltage or the fuel utilization increases, enabling the power output to be increased. The turbine power output also increases due to increased total inlet fuel flow. The system efficiency is in the range of 60 to 65%, and it increases as the cell voltage or fuel utilization increases.

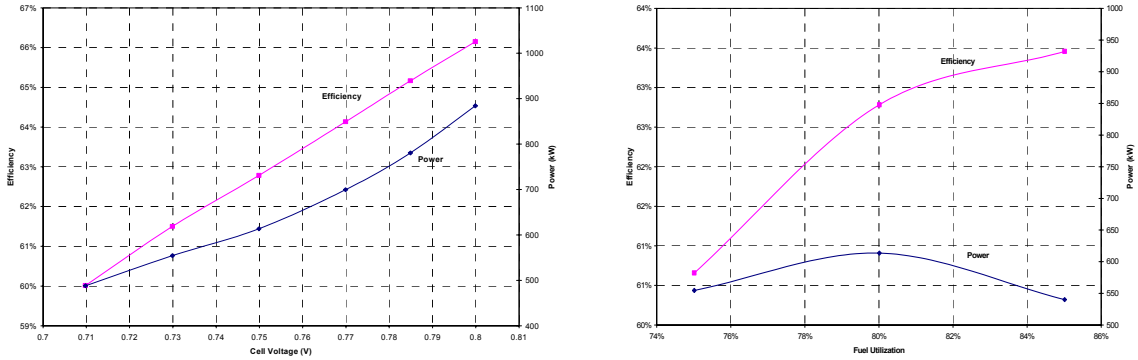

Figure 1 Sensitivity of System Efficiency and Power due to Cell voltage and Cell Utilization for Concept 1 (at 80% fuel utilization and 0.75 V)

The sensitivity of cell voltage and stack fuel utilization on systems efficiency and net power output for concepts 2, and 4 are shown in Figure 2 and Figure 3. A summary of the analysis results for the four concepts is shown in Table 1 and Table 2. The range of cell voltage and fuel utilization considered for each concept remained the same at 0.7 – 0.8 volts and 0.70 – 0.85, respectively.

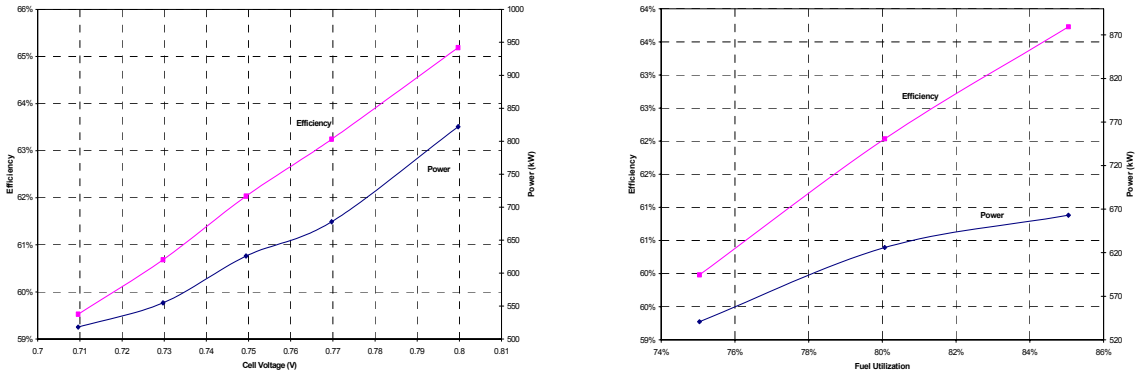

Figure 2 Sensitivity of System Efficiency and Power due to Cell Voltage and Utilization for Concept 2 (at 80% fuel utilization and 0.75 V)

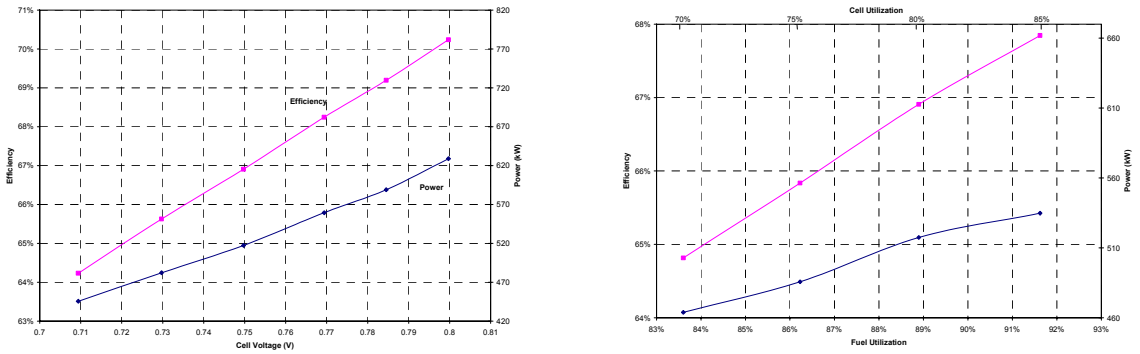

Figure 3 Sensitivity of System Efficiency and Power due to Cell Voltage and Utilization for Concept 4 (at 80% fuel utilization and 0.75 V)

	Concept 1	Concept 2	Concept 3	Concept 4
Net Power, kW	500-900	520-820	200-250	450-650
System Efficiency, %	60-65	60-65	60-65	64-70

Table 1 System Performance Analysis Results Summary

	Concept 1	Concept 2	Concept 3	Concept 4
SOFC Power (kW)	563	581	222	495
Turbine Power (kW)	86	98	17	78
Parasitic Power (kW)	35	53	15	56
Net System Power (kW)	614	626	224	517
System Efficiency (%LHV)	63	62	64	67

Table 2 Systems Performance Analysis Results (at 75% fuel utilization and cell voltage of 0.75V)

The power output from concept 3 is in the range of 200 to 250 kW, less than half of the power achieved by the other concepts. This is mainly due to the low power output from

Parallon 75 caused by a low utilization of air. Because of its low power output, this concept is not analyzed as extensively as the others.

The size of the stack depends on the operating voltage and cell utilization in addition to its power level. Operating cell voltage increases as the current density decreases. Similarly, operating fuel utilization can also be increased by decreasing the operating current density while maintaining the same cell voltage. As the current density decreases, the stack size has to be increased to maintain the same power output, thus increasing the total systems cost. Therefore, there is a trade off between the system efficiency and the total systems cost, which directly affects the cost of electricity.

1.1.2 System Reliability Analysis

The reliability of a plant is the probability that the system will perform its intended function without failure under stated conditions for a specified period of time. It can be defined as

$$reliability = 1 - FOF, \quad (1)$$

in which *FOF* is the forced outage factor, the fraction of time the system is forced to shut down and does not include scheduled shutdowns. The system availability is the probability that the system will perform its intended function at anytime, when used under stated operating conditions. Thus it is the fraction of time the system is operational and includes both forced outages and scheduled outages.

Detail life, maximum and minimum repair time, and service interval data was gathered for all major components for each system concept. This data was used to estimate component reliability and availability. These estimates were then rolled up to determine the overall plant reliability for one year of continuous operation and plant availability over 10 years of operation. The number of forced shut downs as well as service maintenance intervals were also estimated to determine operation and maintenance costs. Table 3 and Table 4 summarizes plant level and subsystem level reliability and availability results for each concept. For these calculations the cell voltage and the cell utilization are fixed at 0.75 and 80%, respectively. This assumption is necessary to determine the heat and mass balance through the system and therefore the operating conditions of all the components.

The reliability of Concept 3 is 0.91, the lowest among the four concepts. The reliability of this concept is driven by its need for a high temperature air preheater.

		Subsystems				
Concept	**Total**	**Fuel Processing**	**Microturbine**	**Power Electronics**	**SOFC**	**BOP**
1	0.995	0.998	0.999	0.999999	0.999	0.999
2	0.994	0.998	0.998	0.999999	0.999	0.999
3	0.907	0.999	0.999	0.999999	0.999	0.910
4	0.997	0.999	0.999	0.999999	0.999	0.9998

Table 3 Reliability Results (at cell voltage of 0.75V and fuel utilization of 80%)

		Subsystems				
Concept	Total	Fuel Processing	Microturbine	Power Electronics	SOFC	BOP
1	0.93	0.99	0.98	0.996	0.995	0.97
2	0.94	0.99	0.98	0.996	0.995	0.98
3	0.94	0.99	0.98	0.996	0.995	0.98
4	0.95	0.99	0.97	0.996	0.995	0.996

Table 4 Availability Results (at cell voltage of 0.75V and fuel utilization of 80%)

Component life information was gathered from several sources. The life of the major components of the turbo-machinery was extracted from the detail life analysis reports on the Parallon75 components. The heat exchanger and the other balance of plant data were gathered from publications on previous development programs, including the advanced DOE micro-turbine program and heat exchanger programs. This data has been supported with information gathered from the Internet. The stack and fuel processor life numbers are based on current engineering knowledge and expert opinion.

The basic assumption behind the reliability model is that the components realize wear in time and the probability of failure is not constant over time. Therefore, the Weibull probability of failure is used. The Weibull slope for all components in this study is between 1 and 4, indicative of increasing probabilities of failure as time increases. In such cases, it has been shown in practice that a scheduled replacement may be cost effective. Consequently, in availability calculations when a maintenance interval is identified for a certain component, the component is assumed to be replaced with a new unit and the component life used in the overall plant reliability is assumed to be reset.

A simple rule of thumb was used to estimate the life of high temperature components and also the temperature dependence of their life. The nominal life of these components were assumed to reduce to half their original life for every 25 degree F increase in operating temperature. This rule of thumb assumes no change in materials from the baseline case and is based on expert judgment.

The availability spreadsheet uses a Monte Carlo simulation to estimate the expected plant availability, the standard deviation of the availability calculation, and the expected number of forced and scheduled plant outages. This analysis assumes a normal probability distribution for the life, i.e. a Weibull distribution with beta set at 1.0. This spreadsheet also requires input of the repair time duration for the availability calculation.

1.1.3 System Cost Analysis

The first cost of the overall system for each system concept was assessed using a cost roll-up model. Component specifications, obtained from system performance analysis, were used to estimate component sizing and then cost. Cost estimates have been made on all major components including the micro-turbine, stack, fuel processor, and the Balance-of-Plant (BOP). The BOP includes the thermal management sub-system, the air, fuel and water delivery sub-systems, and the controls and power electronics subsystems.

All cost estimates have been based on a production volume of 500 units/year or approximately 250 MW per year.

For sub-systems requiring significant technology development, a bottom-up cost model approach was used. For example, a dedicated stack cost model was constructed with the capability to conduct sensitivity analyses. The cost model itemizes the cost into four major components: materials, labor, equipment, and facilities costs. These costs are estimated based on the number of cells and stacks to be build. The total number of cells and stacks are estimated based on a stack performance model. The model makes a projection of the stack performance in the near future. The fuel processor cost was estimated to be the same as that of the stack. This is consistent with TIAX estimation.[1]

Cost estimates for sub-systems containing, to a large degree, currently available technology were derived from quotes obtained from vendors. Adjustments were subsequently made to these quotes to ensure a consistent cost basis. These adjustments were based on engineering judgment. Cost information contained in vendor catalogs were also used as a guide. This approach was used on the micro-turbine, air, fuel and water delivery subsystems and other balance-of-plant (BOP) components. Quotes from vendors, compiled previously for all Parallon 75 micro-turbine, were used as the basis for many of the BOP parts.

Concept No.	**1**	**2**	**3**	**4**
Systems Cost, $/kW	545	563	855	646

Table 5 System Cost Results (at cell voltage of 0.75V and fuel utilization of 80%)

Results from the cost model are summarized in Table 5. The cost ranges from $545/kW to $855/kW. Concept 3 has the highest cost per kW because its power output is low compared with the other concepts.

1.1.4 Cost of Electricity Analysis

The Cost of Electricity (COE) model integrates the performance, reliability, and the cost models. A schematic of the information flow is shown in Figure 4. COE is composed of three parts: the cost of fuel, capital cost, and the cost of operation and maintenance.

[1] "Scale-up Study of 5 KW SECA Modules to a 250 kW System", TIAX LLC Final Report to DOE/NETL, Reference: 74313, June 10, 2002

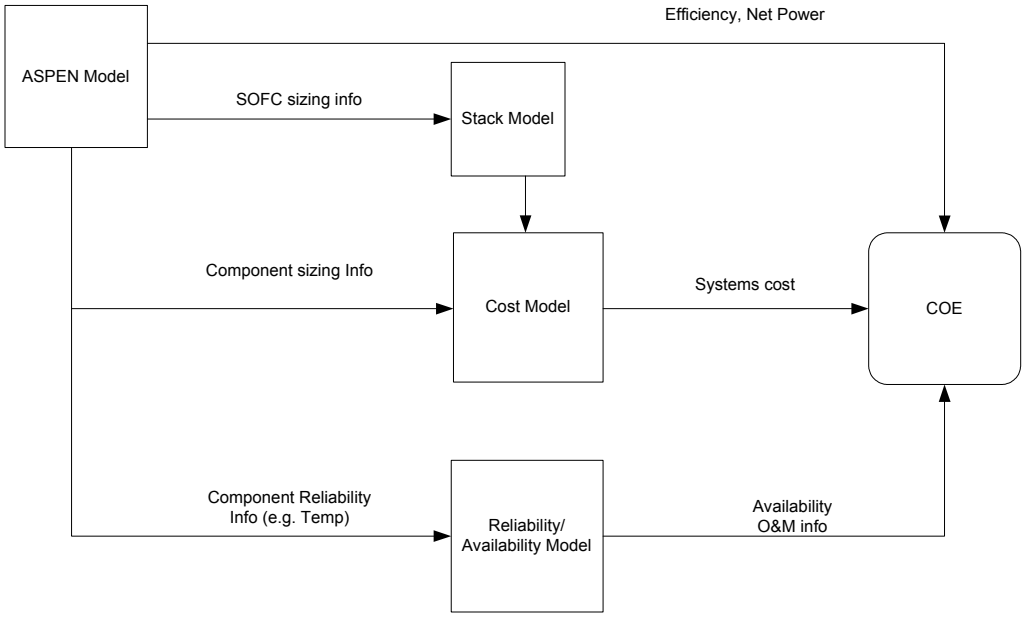

Figure 4 Schematic of the Integrated COE Model

The capitalized cost of the system includes the system manufacturing cost, the installation cost, the other costs associated with installation and operation startup (such as foundation and civil works, and safety systems, etc.) and the owner's costs (owner's engineer, finance costs, etc). The system manufacturing costs, including the microturbine, the stack, the fuel processor, and the Balance-of-Plant (BOP), are estimated in the cost model. The other costs are estimated to be about the same magnitude as the manufacturing costs.

The fuel cost is computed from the total fuel used and the unit cost of fuel. The total fuel used is related to the power plant system efficiency as well as the total power output. The efficiency and net kW output are estimated using ASPEN Plus steady state model. The cost of the natural gas depends on many factors and fluctuates day to day. The historical price of natural gas is shown in Figure 5. The price ranges from $2 to $16/MMBtu-HHV. In this analysis it is assumed to be $6/MMBtu-HHV.

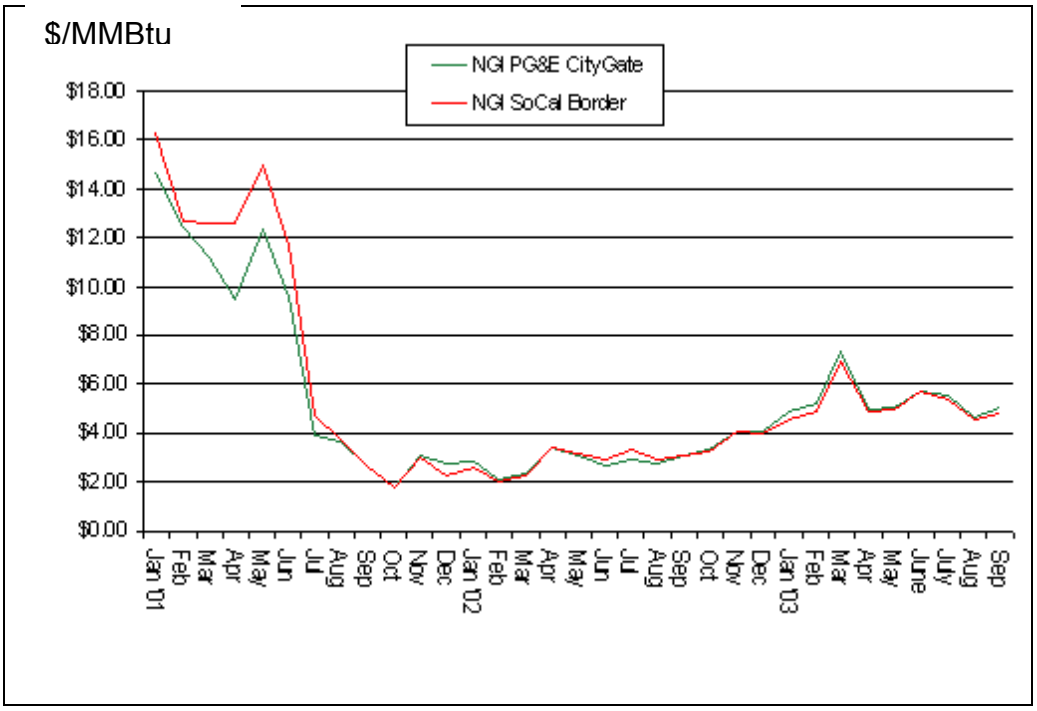

Figure 5 Historical Natural Gas Price[2]

The operation and maintenance cost are related to the cost and frequency of part replacement and maintenance. The frequency of service is computed using the component availability model described above. The frequency of parts replacement was obtained statistically and the replacement costs were estimated.

Results from the COE model are summarized in Table 6. The cell voltage and the cell utilization are fixed at 0.75, and 80%, respectively for this analysis. The COE of Concept 3 is the highest as a result of its highest capital cost.

Concept No.	1	2	3	4
COE, ¢/kW	8.4	8.1	11.8	8.4

Table 6 Summary of COE Results (at cell voltage of 0.75V and fuel utilization of 80%)

Cell voltage and fuel utilization sensitivity on COE have been evaluated. The results for concept 1, 2 and 3 are summarized in Figure 6, Figure 7, and Figure 8. The cell voltage sensitivity trend on COE is the same as that of cell utilization. At low voltage or utilization the system efficiency is low and the cost of fuel drives the COE high. At high voltage or utilizations the capital cost of the system drives up a high COE. The capital cost is high because more cells has to be added in order to compensate performance penalty as a result of high fuel utilization. In the case of high cell voltage, more cells

[2] Source: Bmarkenergy.com

have to be added because of decreased power density as a result of increased cell voltage. The minimum COE occurs approximately at a voltage of 0.75 V and a fuel utilization of 0.8 for concept 1 and 2. For concept 4, the minimum occurs at a fuel utilization of 0.75. However, the COE difference at fuel utilization of 0.75 or 0.8 is very small.

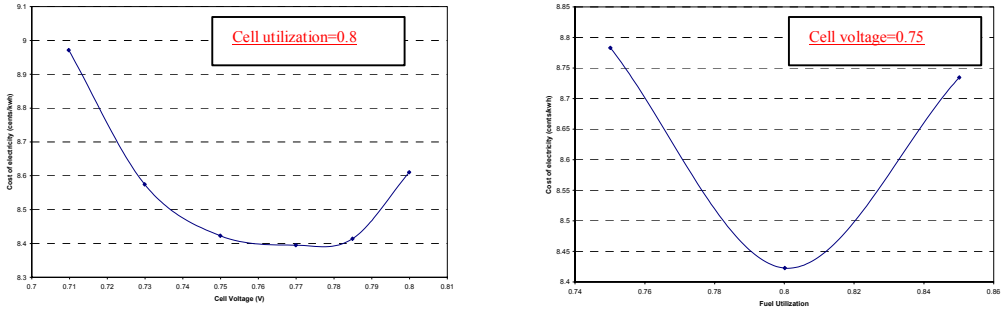

Figure 6 Cell Voltage and Fuel Utilization Sensitivity on COE for Concept 1

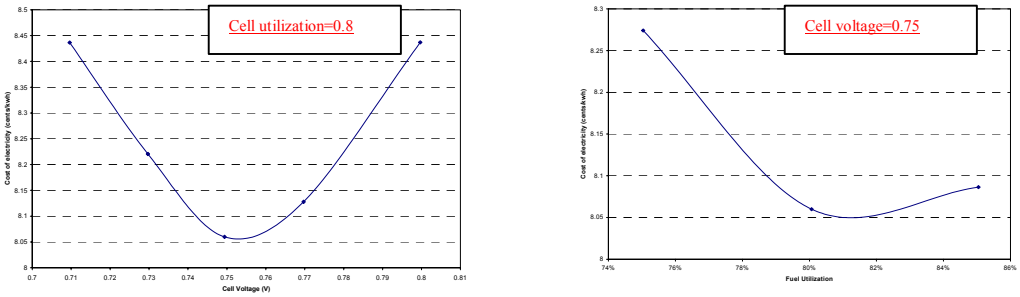

Figure 7 Cell Voltage and Fuel Utilization Sensitivity on COE for Concept 2

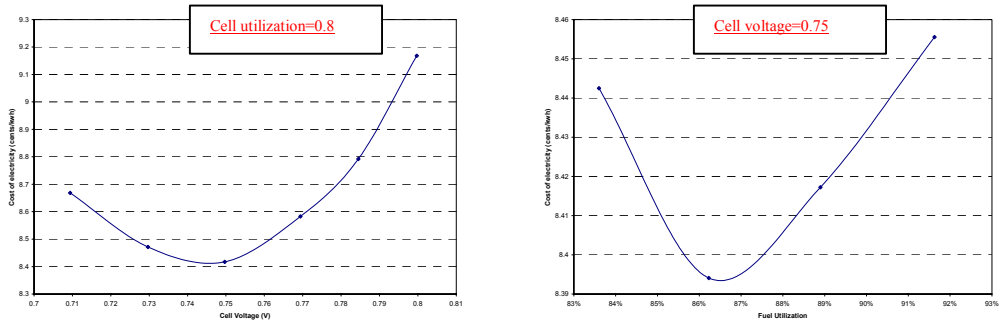

Figure 8 Cell Voltage and Fuel Utilization Sensitivity on COE for Concept 4

1.1.5 Concept Downselection and Summary

The system concept down-selection is based on system efficiency, reliability, cost, and the cost of electricity (COE). The analysis results are summarized in

	Concept 1	Concept 2	Concept 3	Concept 4

SOFC Power (kW)	563	581	222	495
Turbine Power (kW)	86	98	17	78
Parasitic Power (kW)	35	53	15	56
Net System Power (kW)	614	626	224	517
System Efficiency (%LHV)	63	62	64	67
Reliability	0.995	0.994	0.907	0.997
Availability	0.925	0.940	0.938	0.948
System Cost ($/kW)	545	563	855	634
Cost of Electricity (c/kWH)	8.4	8.1	11.8	8.4

Table 7. Results are reported with minimum COE. Concept 2 has the lowest COE, but concept 4 has the highest system efficient.

Design for six sigma tools were used trading cost with efficiency. The system variables used to down select a system concept included systems efficiency, availability, and COE. As shown in Table 8, concept 4 received the highest score

	Concept 1	**Concept 2**	**Concept 3**	**Concept 4**
SOFC Power (kW)	563	581	222	495
Turbine Power (kW)	86	98	17	78
Parasitic Power (kW)	35	53	15	56
Net System Power (kW)	614	626	224	517
System Efficiency (%LHV)	63	62	64	67
Reliability	0.995	0.994	0.907	0.997
Availability	0.925	0.940	0.938	0.948
System Cost ($/kW)	545	563	855	634
Cost of Electricity (c/kWH)	8.4	8.1	11.8	8.4

Table 7 Summary of System Results

DOE Hybrid Conceptual Design

Pass	Marg	Fail
1	0.5	0

				System		
				Efficiency	Availability	Cost of Electricity
			Importance	1	1	1
			USL			8
			LSL	65	96	
			Tolerance	2	2	0.5
			Units	%	%	cents/kwh
	No.	Concepts	Score			
☐	4	Concept4	0.67	66	94.8	8.4
☐	1	Concept1	0.33	63	92.5	8.4
☐	2	Concept2	0.33	62	94	8.1
☐	3	Concept3	0.17	64	93.8	11.8

Table 8 Design Trade Off Results

1.1.6 Part-Load performance analysis of the down-selected concept

Following the down selection of the concept system, its performance at partial loads was analyzed. The system performance model was amended for this purpose by inclusion of component performance maps or estimates, particular to the down-selected concept.

The following assumptions were made:

(1) The Parallon75 recuperator is used. The recuperator performance maps available from Parallon75 test results were included in the model. The recuperator pressure drop curves were also included in the model.

(2) The fuel cell model was adjusted to reflect the recent changes to the cell baseline.

(3) The natural gas compressor efficiency was adjusted to lower numbers at partial loads, shown in Table 9. Since no performance maps are available for this component, conservative estimates were adopted.

(4) The effectiveness of the steam generator, the reformer and the reformate heaters were set to constant values equal to those at the peak power. This is a conservative assumption as the effectiveness of a heat exchanger is likely to improve at lower flow rates due to a longer fluid residence time in the heat

exchanger. This assumption is only valid at steady state and for a limited range of power loads because the bypass flows required to control heat exchanger outlet temperatures will likely be significant at unsteady and/or low power conditions. This assumption will be revised and updated during the detailed design phase when heat exchanger maps are available.

(5) Pressure drops through the system were calculated at partial loads using Aspen's pipe model. The pipe geometry will be adjusted when the piping system design is completed during the detailed phase.

(6) The SOFC pressure drop was conservatively assumed to be about 4.5% of the inlet pressure.

Fuel Flow, kg/sec	Pressure Ratio	Isentropic Efficiency	Mechanical Efficiency
0.0011	1.45	0.55	0.85
0.0037	1.99	0.60	0.85
0.0097	2.89	0.65	0.85
0.0158	4.19	0.70	0.85

Table 9 Natural Gas Compressor Operating Points

The performance model was used to analyze the system performance at the following Parallon75 shaft speeds: 35 krpm, 45 krpm, 55 krpm, and 64.76 krpm (the design point corresponding to peak power). The system power plot is shown on Figure 9.

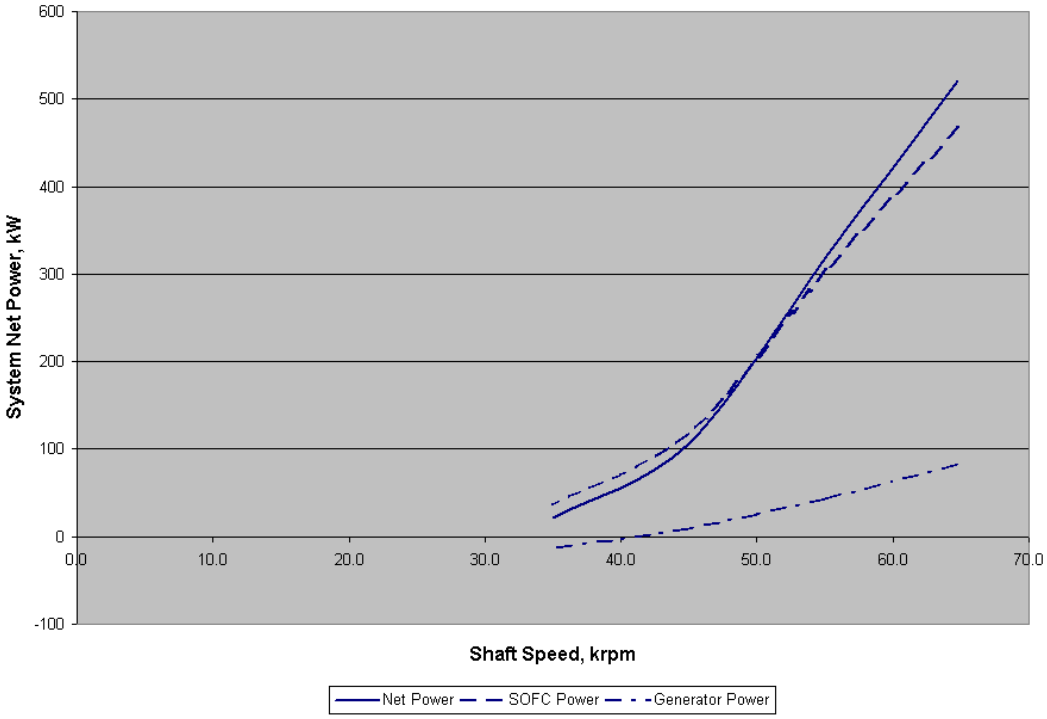

Figure 9 System Power as a Function of the Parallon75 Shaft Speed

Note that the net power is a steep function of the shaft speed. This implies that the system is likely to operate at a speed close to the design speed as long as the power load does not significantly deviates from the peak load.

The microturbine generator power on Figure 9 is negative for shaft speeds below approximately 40 krpm (however, the net system power is still positive). This has implications for the start-up strategy, as the Parallon75 system will have to be operated in the turbocompressor mode rather than the microturbine mode. In other words, the generator would be operated as a motor to drive the compressor. It is recommended to operate the system above 40 krpm at all times in normal operations, if possible to avoid complicated and expensive controls and power electronics solutions.

It should be noted that the control scheme at part loads may have some differences from the peak load control scheme. Particularly, the recuperator inlet temperature requirement was found to have an effect on the average fuel cell temperature at part loads. Since the system operating pressure declines at lower speeds, the turbine pressure ratio is lower as well, which results in higher turbine outlet temperatures. Also, the compressor outlet temperatures are lower because of the lower compressor pressure ratio. This results in a lower fuel cell cathode inlet temperature.

The system efficiency plot is shown on Figure 10. Note that the system efficiency remains relatively flat for the net power higher than about 250 kW (or Parallon75 shaft

speed above 50 krpm). The system power in this region is a strong function of two parameters: (1) the single-cell voltage (the higher the voltage, the higher the system efficiency); and (2) the SOFC specific power, i.e. the ratio of the SOFC power to the cooling air flow rate (the higher the specific power, the higher the efficiency). The voltage rises at lower power loads because the SOFC stack operates at a lower current density. However, this rise is tempered by the decreasing fuel cell temperature and pressure at part load as was discussed above. On the other hand, the specific power tends to decrease with decreasing speed due to the recuperator temperature constraint. The combination of these effects results in a relatively flat efficiency line at higher part loads. However, the SOFC specific power decreases at a faster pace with decreasing system power, which eventually results in lower efficiencies at low part loads.

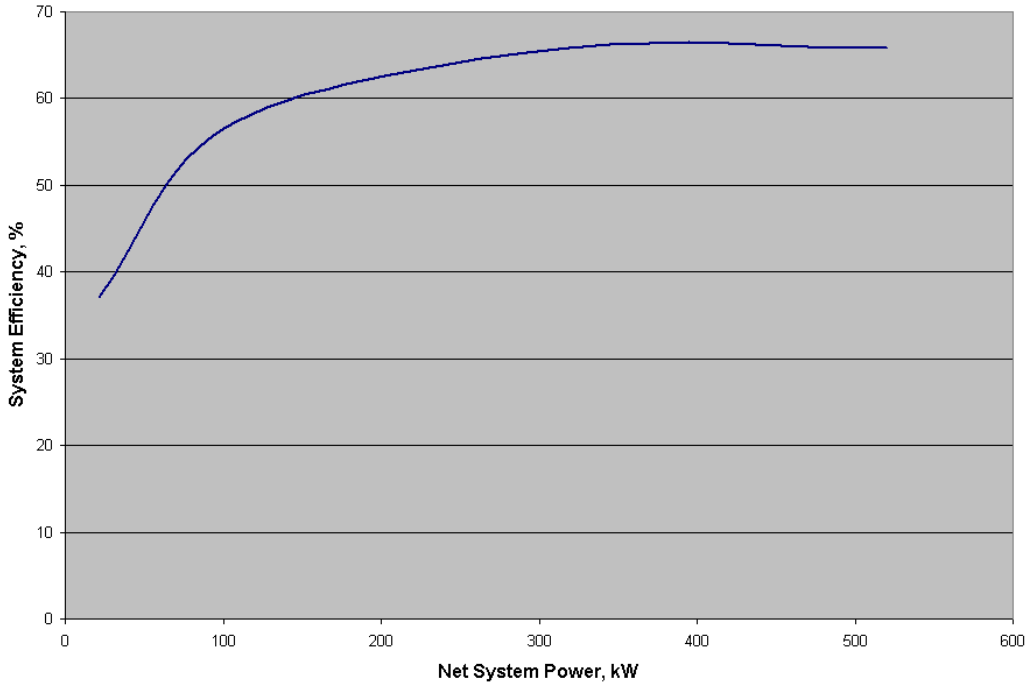

Figure 10 System Efficiency as a Function of Net System Power

1.2 Control System Development

The control system development focused on the following two areas: control system trade studies and conceptual control system design. The objective of the control system trade studies was to develop a better understanding of the controllability of the proposed full-scale system and investigate strategies for controlling the proposed system. The control system trade studies identify key controllability issues and are used to develop the conceptual control system design.

For these studies, controllability goals and objectives were established and the impact of the system design on controllability was evaluated. In addition, the trade studies

helped prioritize the controllability issues based on system requirements. These trade studies provided feedback to the overall system design so that it could be adjusted to improve its potential operation.

1.2.1 Control System Trade Studies

Several control system trade studies were brainstormed and prioritized using a Six Sigma tool, the Quality Function Deployment (QFD). This QFD prioritized the trade studies by ranking each with respect to their influences on major system design changes, system cost, system performance, and system reliability, as well as the maturity of the tools needed to execute the trade study. The transient response trade study and bypass temperature control trade studies were significant enough to warrant investigation early in the program. The stack performance sensitivity trade study was not addressed due to the immaturity of the system design and the availability of the part-load model needed for the study.

A dynamic system model developed in Matlab/Simulink, was used to conduct the control system trade studies. This model was assembled using GE HPGS' Dynamic Fuel Cell Component Library. The model was verified by comparing its results with the results from the Aspen steady state system performance model of the full system. The full system model or an appropriate subset of the system model was used in each of the control system trade studies discussed below. The combined conceptual control system design was subsequently implemented and validated with the full system model.

1.2.1.1 Bypass Temperature Control

The objective of the bypass temperature control trade study is to determine the location and necessity of bypasses for temperature control during start-up, shutdown, normal operation, and load transitions. During this trade study, the conceptual control system design was revisited to explore different concepts for temperature control. Control strategies were evaluated based on:

- Number of bypass valves
- Location and temperature of bypass valves
- Impact on system capital cost
- Impact on system efficiency
- Controllability/Stability at setpoint
- Response time

The bypass temperature control study will be discussed first in terms of cathode temperature control and then in terms of anode temperature control. These trade studies were performed on the downselected system, system concept 4.

1.2.1.1.1 Cathode Temperature Control

There are two strategies that may provide adequate control of the cathode inlet temperature:

A. Bypass hot side of recuperator

B. Bypass cold side of recuperator

Both strategy A and strategy B have the same influence on the cathode inlet temperature. However, since strategy B requires a lower temperature it was selected as a candidate for further investigation.

Simulation studies were conducted using the full dynamic system model to evaluate the performance of the bypass control and tune the cathode inlet temperature controller. While the cathode inlet temperature does not perfectly track the setpoint, the performance of the control strategy is considered acceptable. One risk identified is that the cathode inlet temperature would drop below the lower specification limit if the airflow is greater than 10% of its design point flow rate for more than 30 minutes. However, violation of the lower specification limit may be avoided by decreasing the fuel utilization setpoint (thereby increasing the temperature of air exiting the air preheater) or actively heating the stack. These risk mitigation strategies will be investigated further in subsequent phases of the program.

1.2.1.1.2 Anode Temperature Control

Four strategies were considered to provide adequate control of the anode inlet temperature:

A. Bypass cold side of fuel preheater

B. Bypass cold side of fuel processor preheater

C. Bypass fuel to the fuel processor

D. Bypass cold side of reformate preheater

These strategies were prioritized using a Six Sigma tool. The strategies were qualitatively evaluated against key elements that are considered critical to quality (CTQ's) for the control strategies. Strategy D is expected to have a strong influence on temperature but requires a high temperature valve. Strategy A does not require a high temperature valve but has a weak influence on anode inlet temperature. Strategy B has a weak influence on anode inlet temperature, but may be important for fuel processor and reformate composition control. Strategy C may have limited utility unless the stack's internal reforming capability is large and the temperature impact on the stack is explicitly considered in the control algorithms. Strategies A and D were selected as the candidates for further analysis.

	Strategies						
CTQ's	Importance	D - Reformate Preheater Bypass	A - Fuel Preheater Bypass	B - Fuel Processor Preheater Bypass	C - Fuel Processor Bypass		Total
Valve Temperature	5	l	h	l	l		60
Strong Influence on Temperature	4	h	l	m	l		56
Robustness/Controllability	3	h	m	m	l		48
Fast Response on Anode Temperature	2	h	l	m	m		32
Total		86	60	32	18		

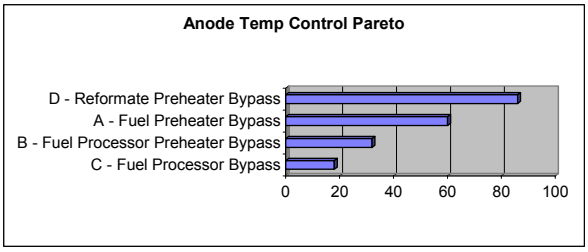

Figure 11 Rank for Anode Temperature Control Strategies

A Matlab/Simulink dynamic subsystem model containing the fuel preheater and bypass, fuel processor, reformate preheater and bypass, and stack is used to analyze the two down selected control strategies. For both strategies, the bypass valve is used to control stack anode inlet temperature with a proportional plus integral (PI) controller.

For Strategy A, the fuel preheater bypass controller is turned on at the full power condition and is not able to maintain an anode inlet temperature with the bypass valve at 100% open. For Strategy D, the reformate preheater bypass controller is turned on at the full power condition and is also not able to maintain an anode inlet temperature, but by a less margin than strategy A. The bypass valve is also 100% open, but direct control of anode inlet temperature provides a more favorable response without the process time delays and thermal lags of the fuel processor that exist with Strategy A. While neither strategy was able to maintain the desired setpoint, strategy A is considered more effective and therefore selected.

Simulation studies were subsequently conducted using the full dynamic system model to evaluate the performance of the reformate preheater bypass control (strategy A) and tune the anode inlet temperature controller.

1.2.1.2 Transient Response

This trade study focused on SOFC/microturbine hybrid system transient behavior. The results from this trade study will be used to develop load sharing control techniques for the microturbine-generator (MTG) and SOFC power systems during load transients and disturbances. A simplified hybrid system model was used to examine the major system components with the goal of qualitatively characterizing gross dynamic interactions. A novel control method has been developed that allows the hybrid system, with power being generated by both the SOFC and MTG, to follow a demanded, transient power setpoint and thus follow load changes in a controllable fashion.

The system concept evaluated in this trade study was based on Concept #1. Major components such as the SOFC, turbomachinery, recuperator, stack heat exchanger, and depleted fuel oxidizer were included in the dynamic system model.

The following recommendations can be made from the results of this trade study.

Minimize Internal Volumes - Internal volumes have a direct impact on controllability, especially during load transitions. The larger the internal volumes of the components and piping of the hybrid system, the more drastic the system responses are to a load change or disturbance. The system can transition faster between load demand setpoints when the volume is minimized. Larger volumes will decrease the transition speed away from the entitlement ramp rate.

Minimize Component Pressure Drops - Each component pressure drop contributes to losses in system efficiency. In addition, larger pressure drops leave less surge margin for the compressor and slow system response—especially during a load decrease. A reliable load transition necessitates adequate margin from surge as disturbances not modeled in this study may require additional margin to keep the compressor from surging.

Incorporate Blow-off Valving - As stated earlier, the volumes associated with the working fluid have a profound effect on the transient performance of the hybrid system. The largest of these will likely be associated with the pressure vessel that will house the SOFC stack. Large volumes slow the system response in that they act as a pressure capacitance, storing working fluid mass. When the system reduces power, the pressure inside the vessel does not decay instantaneously as the MTG speed is reduced. This causes the MTG Compressor performance running line to move towards the surge line. The surging phenomenon is caused by the inability of the compressor discharge fluid momentum to overcome the pressure gradient across the compressor wheel (without momentum, the fluid will tend to flow from high to low pressure, backwards over the compressor wheel—the opposite direction required to operate the hybrid system). In order to reduce the likelihood of surging, the pressure in the SOFC stack containment vessel should be reduced quickly upon MTG deceleration, so that the running line remains away from the surge line. One way to increase the speed in which the pressure vessel volume discharges would be to incorporate a blow-off, or pressure relief valve. This would, if sized correctly keep the compressor away from surge during a load reduction event. The correct placement of the valve, either before or after the stack, should be studied further as a way to increase the transition speed, at least for load reduction.

Incorporate Bypasses - Because of the nature of the single shaft MTG, the turbine expander outlet temperature (TOT) decreases with increasing airflow and system power. This will serve, due to recuperation of the system exhaust heat, to lower the SOFC stack inlet temperature as airflow increases and increase stack inlet temperature as airflow decreases. Thus, there will be one particular airflow and associated enthalpy that will match the SOFC stack for a given current drawn, precluding any variation in stoichiometric ratios. For flexibility in operation (i.e. variation of air stoichiometry), bypasses around the stack and/or recuperator may need to be incorporated to provide an increased temperature control capability for off-design conditions.

There are some risks associated with the recommendations of the transient trade study. It must be understood that this was a simulation with many simplifying assumptions. The goal, in this case, was to identify trends that should be explored further in the

Preliminary and Detailed designs. The quantitative values may not be representative of an actual system, but were used to qualitatively identify hybrid system performance.

One simplification that might have an effect on performance was the transient response of the fuel reformer. This study assumed that the thermodynamics of the fuel reformation process is accounted for, but does not specify the fashion (external, internal, steam, partial oxidation, etc.). A significant limitation might be imposed on the fuel utilization algorithm should the reformer play a critical limitation in transient response.

Another risk was the stack performance model. The current neural network model does not vary performance based on fuel composition—only on overall fuel utilization. It is well known that SOFC performance is dependent on fuel composition as well as fuel utilization. Only hydrogen fuel diluted with nitrogen has been mapped in the current SOFC performance model. Therefore, in addition to the thermodynamic response of the reformer stated above, the fuel composition entering the SOFC stack may impose transient effects not modeled in this study.

The heat loss from the system was assumed to only take place through the SOFC stack pressure vessel wall. Both the value and the location of the actual system heat rejection may have a profound effect on operation and thus might affect the actual transient and steady-state performance of the hybrid system.

1.2.1.3 Control System Trade Study Summary and Conclusions

Several areas were investigated as part of the control system trade studies to identify controllability issues that could influence the conceptual system design and to begin to define how to control the proposed hybrid system. The most important conclusion drawn from these trade studies is that Concept 4 can be controlled.

The transient response trade study looked at the hybrid system and established a preliminary estimated load-change ramp rate of 1500 W/s if the system volumes are minimized. There were many assumptions that went into this estimate and additional analysis with more detailed component information will be needed in subsequent phases of the program to determine the true entitlement of the system. The control strategy developed in the transient response trade study showed that the temperature of the SOFC can be adequately controlled using current draw, with the power demand being met based on feedforward setpoint controls for airflow and some trimming with fuel utilization. This strategy shows great promise in minimizing the temperature fluctuations of the SOFC stack.

1.2.2 Conceptual Control System Design

The conceptual control system design for the full-scale system was updated with the results of the control system trade studies. The control structure underwent few changes as a result of this update.

The control structure is divided into two subgroups, the supervisory controls and the active controls. The supervisory controls perform the following functions:

- Translates load demand, user commands, and system status into setpoints for active controls
- Manage operating modes
    - Startup
    - Normal Operation
    - Shutdown
    - Emergency Stop
- Manages Built-In Test (BIT) and alarms

The active controls perform the following functions:

- Feedforward control for fast transitions between setpoints
- Feedback control for disturbance rejection and improved setpoint tracking

The feedforward control takes advantage of a priori information on the system operation to improve the transient response and stability of the system. An example of this would be the setting for the cathode temperature control valve being scheduled as a function of fuel cell power. Therefore when the fuel cell power is commanded by the controller, the appropriate valve position is also commanded. The feedback action of the control system would then fine-tune the position of the valve to achieve the exact cathode inlet temperature setpoint. The feedback portion of the control therefore provides disturbance rejection and robustness to variation in the process or components.

Due to the complexity of the system and its numerous constraints, the supervisory controls must be coordinated with the lower level control loops must also watch all component and system constraints while maintaining the demanded load.

The conceptual control system design has been implemented, tuned, and verified in the full dynamic system model. The supervisory controls have only been implemented to the point of coordinating lower level control loops. The built-in test and health monitoring functions will be added in subsequent phases of the program. The simulation results show the temperature and pressure constraints around the system are satisfied during rabid load changes of 500 W/s. The fuel utilization is not well controlled with load changes causing large deviations from the targeted value of 80%. This will need further investigation in subsequent phases of the program, but is probably due to the fuel flow control and pressure dynamics associated with the long path fuel must travel before reaching the stack. These oscillations can be limited or removed if the load change ramp rate were further limited.

2 TECHNICAL BARRIER RESOLUTION

2.1 High Temperature Heat Exchangers

The objective of this task is to develop, design, fabricate, and test a high temperature heat exchanger capable of operating with high-temperature exhaust gases to heat up air before it is introduced into the fuel cell stack. This report outlined the design and

construction of a demonstration heat exchanger for testing and the analysis of a high temperature heat exchanger for pressure containment and creep life. The pressure containment and creep life analysis is supported with oxidation tests on coupons of representative high temperature materials presented below. Further, the performance testing of a prototypical heat exchanger is also presented below.

2.1.1 Heat Exchanger Design and Construction

The focus of this task was on the development of a high temperature heat exchanger to understand the feasibility of using such a heat exchanger in SOFC-hybrid systems. Consequently, the prototypical heat exchanger design was based on the requirements of the demonstration system. The design point performance requirements and the thermal design of the high temperature heat exchanger was therefore based on the performance requirements of the demonstration system. The specifics of this design are presented in Table 10 and the design is shown in Figure 12.

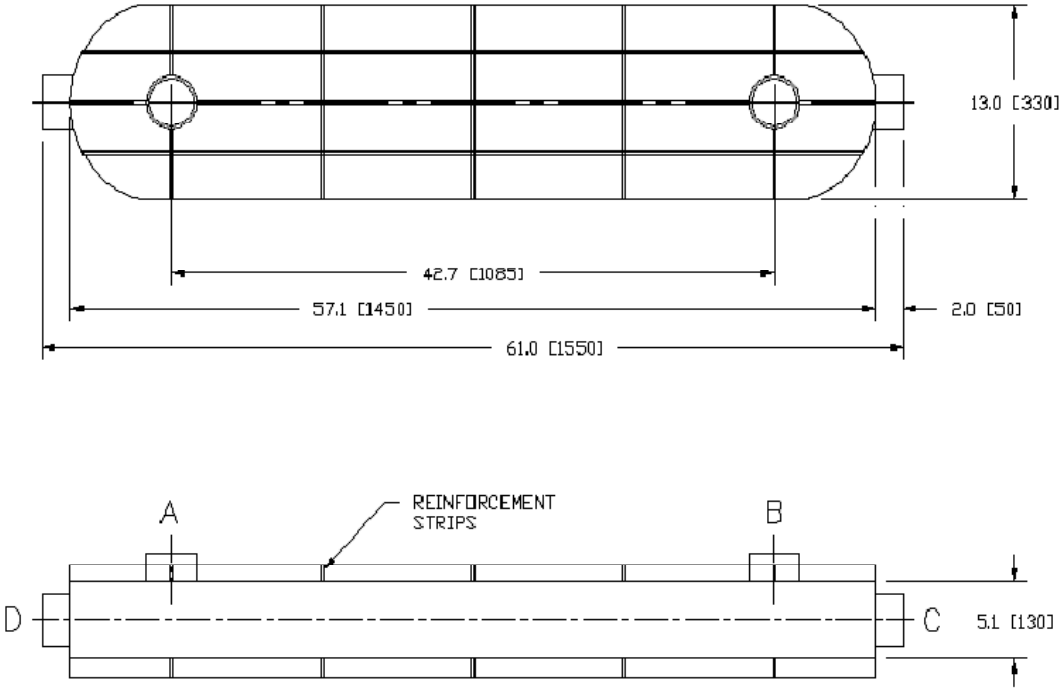

Figure 12 Heat Exchanger Design

Heat Exchanger Operation		
	Hot Fluid	**Cold Fluid**
Flow Rate (lb/min)	9.33	9.52
Inlet Temperature (°F)	308	908
Exit Temperature (°F)	849	430
Inlet Pressure (psia)	38.6	35.4
Pressure Drop (in H_2O)	0.524	0.234
Effectiveness	90%	80%
Heat Exchanger Core Construction		
Construction Type		Inconel 625, Plate-fin, Counterflow
Core Dimensions (inches)		10 x 8.7 x 4.4
No of passages (hot side/cold side)		19/19
Core Weight (lb)		21.1

Table 10 Thermal design of a high temperature heat exchanger

2.1.2 Heat Exchanger Analysis

Analysis was conducted to evaluate the life of the air preheat heat exchanger for the full-scale system at design point operating conditions. The analysis included structural analysis for pressure containment and creep life assessment for the heat exchanger core fins and manifolds. An example of the Finite Element computation field is shown in Figure 13.

The heat exchanger core and four manifolds were all found to have acceptable stress levels for pressure containment. For the gas manifolds, the stresses were calculated from nonlinear stress analysis. Negative stress margins confirmed local yielding in the manifold. However, the strain levels were found to be within acceptable limits.

The life to creep rupture was also estimated for the heat exchanger core and manifolds. The gas inlet manifold pan was found to be the most critical component in terms of susceptibility to creep rupture. However, this can be alleviated with the use of thicker material in the pan. The heat exchanger core design was found to have substantially higher life to creep if made with Inconel 625. Based on an estimated applied stress of 3.5 ksi in the hot passage of the core, the use of Inconel 625 fins yields a life of over 5,000 hours. The results for this analysis is summarized in Table 11.

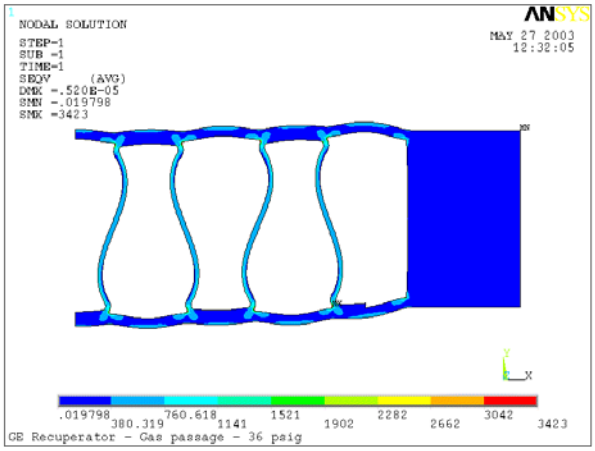

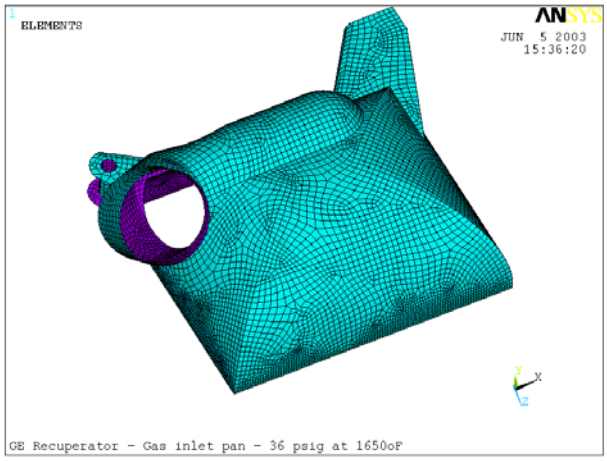

Fins Manifold Pan

Figure 13 Finite Element Models of the Heat Exchanger Fins and Manifold

	18-2 material	Inconel 625
Rupture, LMP [2]	40.5	50.1
Temperature	1650°F	1650°F
Time (hours)	**0.16**	**5547**

Table 11 Preliminary Creep Life Analysis Results

2.1.3 Oxidation Tests

Sixty coupon samples were prepared and placed in three furnaces at different temperatures: 732 °C (1350°F), 800 °C (1475°F), and 900 °C (1650°F). The tested coupons were made with Inconel 625 and Haynes 230 rods. These samples were exposed to the SOFC combustion environment having gas compositions as described in Table 12. Samples were scheduled for removal from the furnace at different exposure times ranging from 250 to 5000 hours. Micrographs showing the oxidation of these samples at exposure times up to 315 hour at the three temperatures is shown in Figure 14. Figure 15 shows similar micrographs for samples removed from the 900 °C (1650 °F) furnace after up to 3000 hours of exposure.

Gas	Approx Partial Pressure at 800 °C (1475 °F)
N_2	0.7922
O_2	0.1039
CO_2	0.0346

H_2O	0.0693
H_2	9.73E-11

Table 12 Approx Gas Composition Used for Coupon Testing

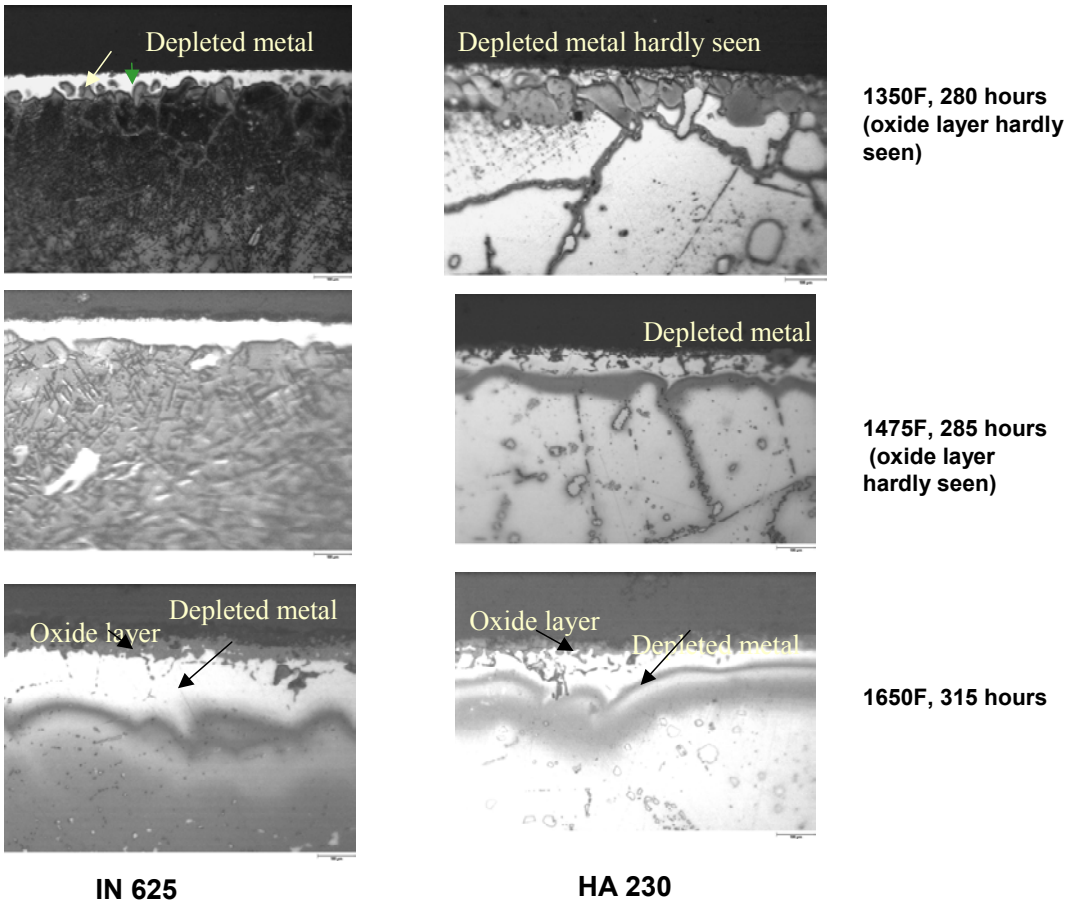

Figure 14 Oxidation Tests of Inconel and Haynes Coupons at Various Exposure Temperatures

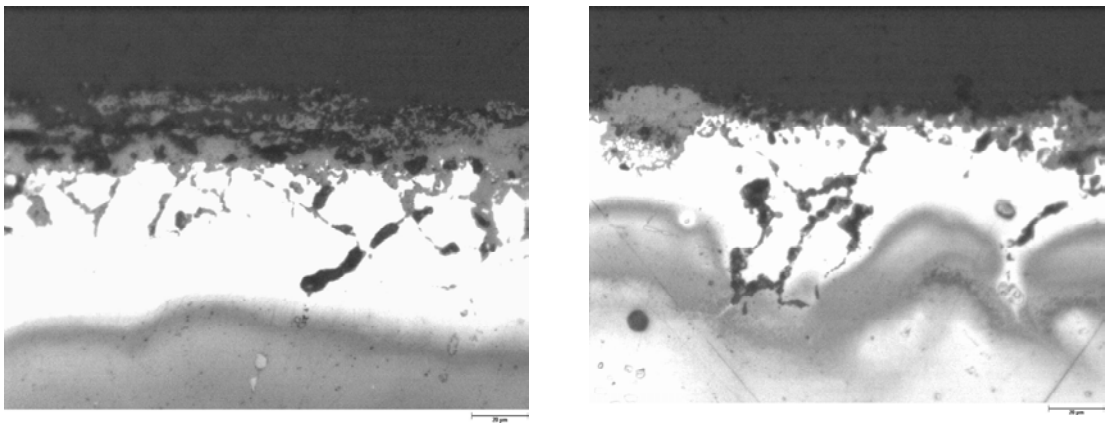

IN 625 exposed at 1650F for 3041 hours **Haynes 230 exposed at 1650F for 3041 hours**

Figure 15 Burner Rig Photographs Showing Oxide Scale, Depleted Metal, and Oxide Penetration

The oxide penetration was measured on samples removed from the furnace and correlated with exposure time. The plots showing attack as a function of time for the three exposure temperatures is provided in Figure 16 through Figure 18.

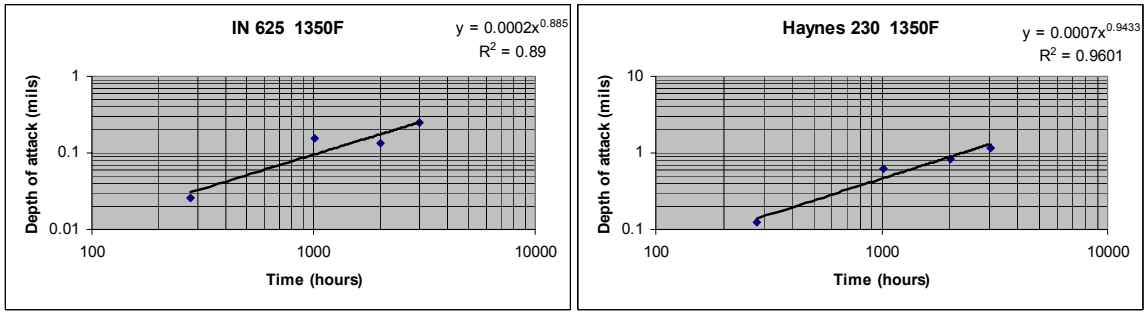

Figure 16 Oxidation Data as Function of Time at 1350 °F

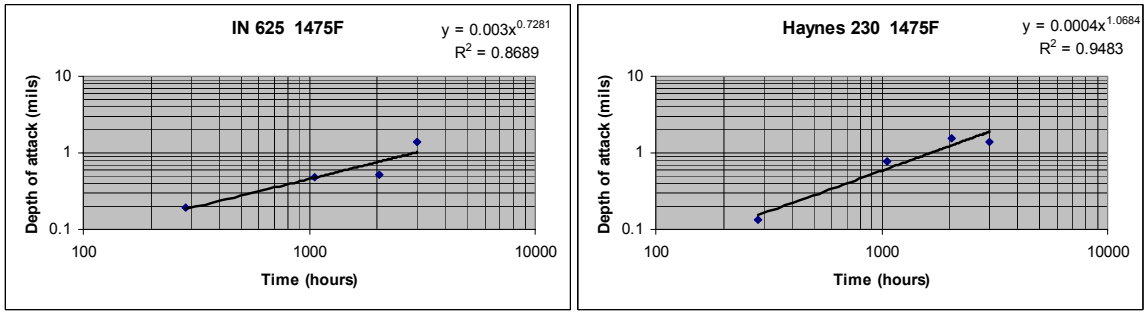

Figure 17 Oxidation Data as Function of Time at 1475 °F

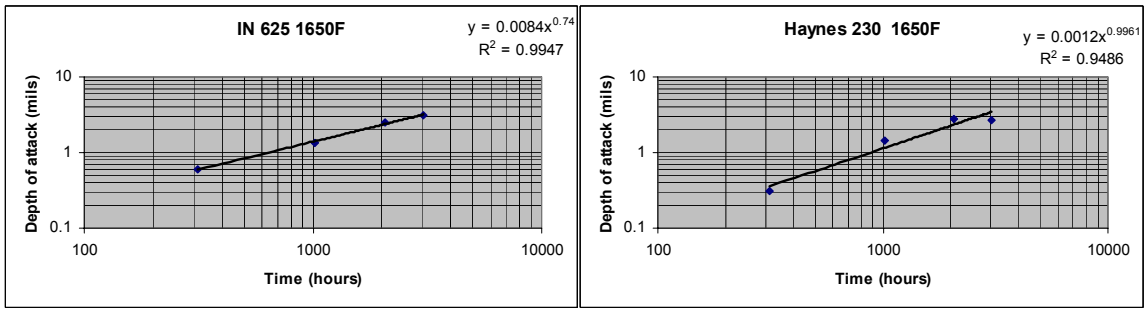

Figure 18 Oxidation Data as Function of Time at 1650 °F

The depth of metal attack used in these plots includes the thickness of the oxide layer and the thickness of the depleted zone from which alloying elements are lost. It should be noted that general literature on oxidation usually is based on the oxide layer alone.

Assuming a required design life of 5000 hours for a high temperature heat exchanger constructed using 0.003-inch thick metal sheets, the data suggests both Inconel 625 and Haynes 230 are suitable for applications up to 730 °C (1350 °F). However, at 800 °C (1475 °F) the Inconel 625 will achieve the design life but Haynes 230 will not.

It should be noted the plots shown in Figure 16 through Figure 18 have been fitted with relatively short exposure data, approximately 3000 hours. Consequently, caution must be exercised in extrapolating this data to longer durations.

2.1.4 Heat Exchanger Tests

A series of performance tests were conducted with the prototypical heat exchanger, described above and shown in Figure 12. The heat exchanger test matrix, which includes pressure drop and thermal performance measurements at various design and off-design operations is shown in Table 13.

Test	Hot Flow Rate (lb/min)	Cold Flow Rate (lb/min)	Hot Inlet Temp (°F)	Cold Inlet Temp (°F)
1	8	8	900	75
2	9	8	900	75
3	10	8	900	75
4	11	8	900	75
5	8	9	900	75
6	9	9	900	75
7	10	9	900	75
8	11	9	900	75
9	8	10	900	75
10	9	10	900	75
11	10	10	900	75
12	11	10	900	75
13	8	11	900	75
14	9	11	900	75
15	10	11	900	75
16	11	11	900	75
17	10	10	1200	75
18	10	10	1400	75
Repeated data points				
19	8	10	900	75
20	9	10	900	75
21	10	10	900	75
22	11	10	900	75

Table 13 Test Matrix for Heat Exchanger Performance and Pressure Drop Test

The heat exchanger test set up is shown in Figure 19. The tests were conducted according to the following process. Flow rates, temperatures, and pressures were measured at the inlet and exit streams of the heat exchanger. At each operation set point the unit was allowed for the unit to achieve steady state conditions. Temperature and pressure measurements were taken at at-least three points within the duct cross-section to ensure bulk average temperatures were being recorded. At the outlet of the heat exchanger a mixer was used to measure the mixed flow temperature. The pressure measurement was measured before the mixer, at the outlet of the heat exchanger. All the data was recorded using Lab View data acquisition system. During the test, no anomalies occurred.

Front view

Left side view

Right side view

Thermocouples in heat exchanger skin

Figure 19 Pictures of Heat Exchanger Test Setup

Table 14 and Table 15 show the sample data taken during the performance test and the results computed from the raw data.

Hot Flow Rate (kg/s)	Cold Flow Rate (kg/s)	Hot Inlet Temp (deg K)	Cold Inlet Temp (deg K)	Hot Outlet Temp (deg K)	Cold Outlet Temp (deg K)	Pressure Drop Hot side (psig)	Pressure Drop Cold side (psig)
0.062	0.061	755.224	299.417	389.619	607.909	1.0	0.4
0.068	0.061	755.716	299.470	389.857	611.529	1.3	0.39
0.077	0.061	755.726	299.435	399.017	617.246	1.6	0.39
0.084	0.061	755.022	299.487	416.106	624.106	1.8	0.4

Table 14 Sample Heat Exchanger Performance Test Data

Hot Stream Mean Temp (deg K)	Cold Stream Mean Temp (deg K)	Qmax (W)	Effectiveness	U
572	454	28304	0.68	20.26
573	456	28220	0.68	20.41
577	458	28332	0.69	20.01
586	462	28308	0.71	19.08

Table 15 Sample Heat Exchanger Performance Results

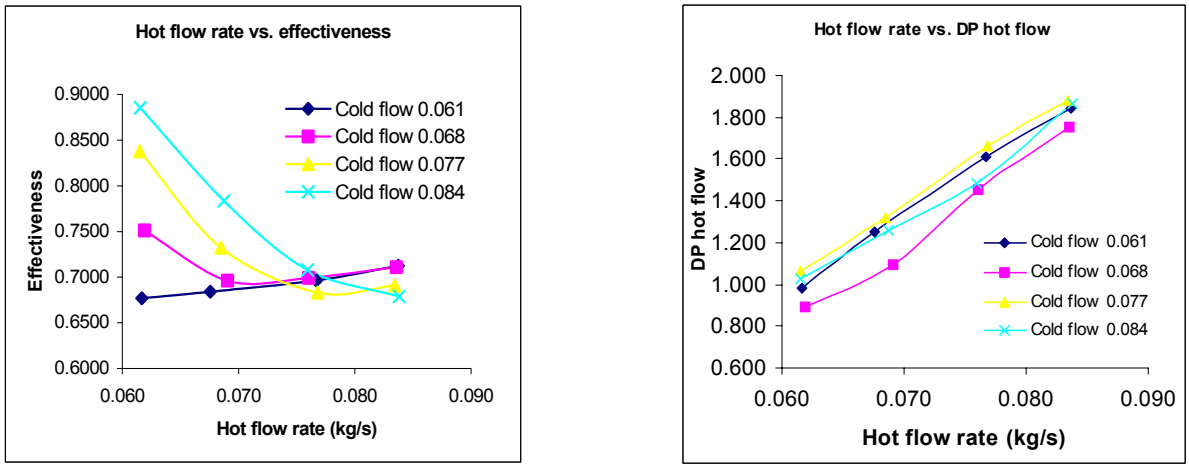

Figure 20 Heat Exchanger Results

Figure 20 summarizes the performance results of the heat exchanger. The heat transfer and pressure drop of the heat exchanger are in good agreement with the design specification of the heat exchanger.

2.2 Pressurized SOFC

Single cell pressurized testing has been performed using two identical pressure vessels that have a stamped vessel rating for 60 psig. These vessels have been used to

conduct pressurized carbon deposition experiments and performance degradation or life tests.

2.2.1 Carbon Deposition Experiments

The use of nickel based anode has many advantages over others in terms of cell support structure (anode-supported cells), fast electrochemical oxidation kinetics (high exchange current density) and high activity toward reformation of fuels (internal reforming of hydrocarbon fuels). Especially, the high internal reforming activity provided by nickel based anodes allows highly efficient cell operation with reduced degree of external reformation, leading to a smaller external reformer. However, one concern with the use of hydrocarbon containing fuel streams is carbon deposition. The problem of carbon deposition is present whenever hydrocarbon containing fuel is employed as anode fuel irrespective of pre-reformation method (such as steam, auto-thermal or partial oxidation reformation).

Carbon deposition is generally observed over non-noble metal catalysts such as Ni, Co and Fe. The carbon deposition rate is impacted by many factors, such as the nature of the catalyst material, the chain length of hydrocarbon fuels, carbon/hydrogen/oxygen (C/H/O) elemental ratio of the fuel stream, and temperature and residence time. Also, the nature of carbon that is deposited (whether it is nanotube, whisker, polymeric, etc..) is dependent on the above mentioned reaction conditions. Generally, higher hydrocarbon fuels exhibit considerably higher rates of carbon deposition.

A fuel stream that shows high carbon element percentage in its C/H/O elemental ratio shows higher thermodynamic driving force toward carbon deposition. Therefore, raising the H and/or O ratio in C/H/O elemental ratio helps to prevent or circumvent environments that lead to carbon deposition. This directly translates to adding more steam or oxygen (or air) to the anode fuel stream for either external or internal reformation. During fuel cell operation, the generation of current is equivalent to transferring oxygen from the cathode stream to the anode stream through the electrolyte. Therefore, the fuel stream composition changes gradually as it travels along the anode flow field. The anode inlet of the cell corresponds to zero current generation and therefore, is more likely susceptible to carbon deposition. Contrarily, fuel stream leaving the anode flow field is relatively rich in O in its elemental C/H/O ratio and therefore, it is far less likely to suffer from carbon deposition, or in other words, is far away from carbon deposition boundary.

The thermodynamic prediction of carbon deposition at 1 atm in a cell running on a simple mixture of methane and steam is depicted in Figure 21. The elemental compositions of the individual anode fuel streams were calculated and plotted in elemental ternary diagram. Also, the composition of anode fuel stream that went through 80% fuel utilization was calculated and plotted on the diagram for comparison. The carbon boundary line shown in Figure 21 was reproduced from literature and it was found to agree well with our thermodynamic calculations. From Figure 21, anode fuel stream of S/C 1.5 (i.e. a simple mixture of H_2O and CH_4 in the ratio of 1.5) is located far below the carbon boundary at 800°C both at the anode inlet and outlet locations, with

fuel utilization at 80%. This implies that all anode regions are safe from carbon deposition. Contrarily, the inlet region of S/C 0.1 anode fuel stream is located above the carbon boundary indicating potential for carbon deposition.

As shown in Figure 21, the elemental ratio of C/H/O changes along the anode flow field such that it can cross the carbon deposition boundary. Moreover, the accompanying internal reforming reaction, aside from current generation, contributes to local temperature changes since the internal reformation reaction is strongly endothermic. These factors make the prediction of carbon deposition in a working fuel cell complicated. In addition, kinetic factors are not taken into account in this thermodynamic prediction. Therefore, it is imperative to experimentally verify the conditions under which fuel cells can be run on hydrocarbon fuels (methane in this study) without the risk of carbon deposition.

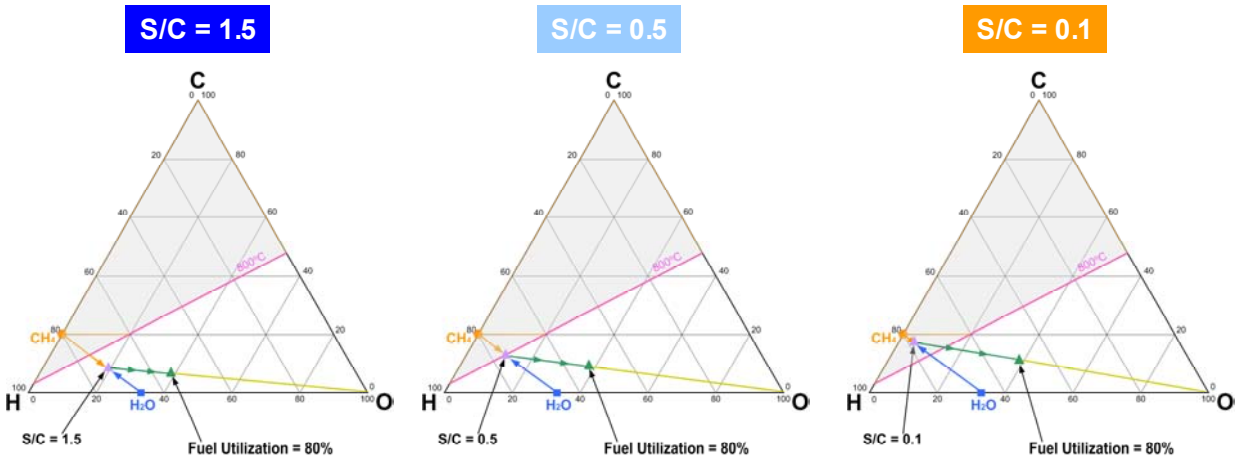

Figure 21: Carbon deposition prediction in fuel cell anode

In this study, the potential degradation of cell performance associated with carbon deposition was experimentally evaluated for both ambient and elevated pressure (44.1 psig). Single cell modules with interconnects operating on a controlled reformate composition were employed and the effect of carbon deposition was observed based on cell performance and stability.

2.2.1.1 Testing Approach

In this task, cells were operated on a number of controlled anode fuel streams and the cell performance was monitored to learn the effect of carbon deposition on cell performance and stability. The cell performance test was conducted at a constant cell load (current) and cell voltage was measured. A drop in cell voltage over time is attributed to carbon deposition over the anode electrode if it exceeds the expected steady state degradation.

Experiments were conducted using 3-inch and 4 3/8-inch circular cells with a sealless radial flow field configuration. In this configuration the anode fuel stream and cathode air stream exhausts were mixed together and combusted inside the vessel after leaving

the cell. Once the cell was assembled, mounted and plumbed for gas feed, it was reduced at two different conditions (25% H2 and 64% H2, respectively) for a predetermined period of time. Then, the cell was conditioned for its maximum performance by applying an electric load for about 20 hours. Once the cell exhibited acceptable performance through cell conditioning, cell testing with a number of simulated anode fuel stream was initiated. At the start of the test the anode fuel stream was wet enough (corresponding to high steam-to-carbon ratio of fuel stream) to ensure that carbon deposition did not occur. During this period the performance and stability of the cell was monitored for a predetermined period of time. Once the cell demonstrated stable operation with the "wet" fuel stream, the anode stream was transitioned to a "drier" (corresponding to low steam-to-carbon ratio) fuel composition and the cell performance and stability was monitored. This process was repeated until cell voltage drop attributed to carbon deposition was observed. The voltage was allowed to continue dropping for a prescribed period of time or until the voltage got as low as 0.55V. This was to ensure that sufficient carbon was deposited for verification purposes. Finally, the cell was put under open circuit condition (with no electric load) and subsequently cooled down under a controlled environment to preserve any carbon deposits. Subsequently, carbon deposits were verified through microscopic surface analysis.

2.2.1.2 Test Set-Up

The testing for carbon deposition was designed to mimic a cell operating within the framework of a hybrid system configuration as shown in Figure 22. Upstream of the cell, methane and steam, with a predetermined steam-to-carbon ratio, is mixed with the anode exhaust recycle stream. Then, this mixture flows through the "Steam Reformer" and "SOFC, Anode" for external steam reformation and power generation, respectively. The anode exhaust out of "SOFC, Anode" is then split into two directions. Part of the anode exhaust stream is directed out of the system for further processing and the other part of the anode exhaust stream is recycled back to the inlet fuel. A closer look at the system configuration reveals that the composition of the anode fuel stream that enters the "SOFC, Anode" is determined by many system design factors, such as steam-to-carbon ratio in the inlet fuel mixture, the steam reformer size and temperature, the cell current density and fuel utilization, and the anode exhaust recycle ratio. In determining system representative anode fuel stream compositions, cell current density and fuel utilization were set at 400mA/cm2 and 80%, respectively. Steam-to-carbon ratio was found to be a major factor that determines the anode fuel stream composition and representative values of steam reformer size/temperature and anode exhaust recycle ratio were used in the calculation of anode fuel stream composition.

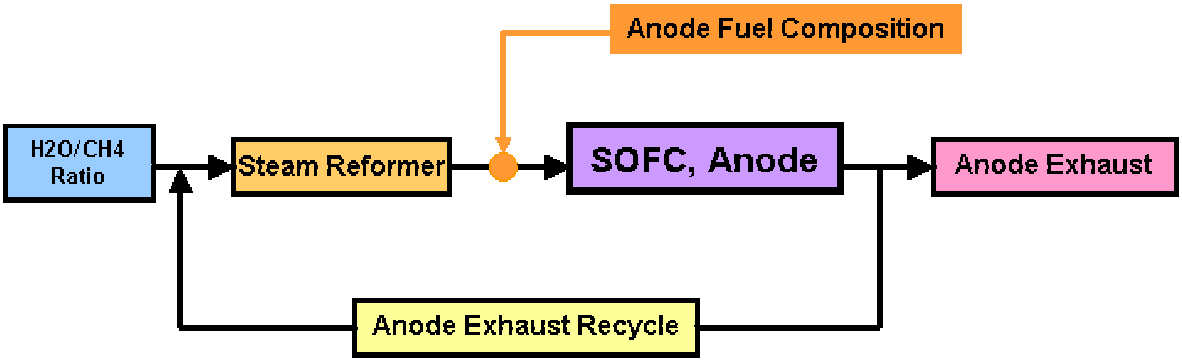

Figure 22: Configuration of fuel cell within the framework of hybrid system design

The anode fuel stream composition was computed using the process described above and calculated using process modeling software and is summarized in Table 16.

S/C	3.0	2.0	1.5	1.0	0.7	0.6	0.5	0.4	0.3	0.2	0.1	0.001
H_2	26.3%	28.6%	30.0%	31.5%	32.0%	32.2%	32.0%	31.9%	31.1%	30.0%	26.6%	4.0%
O_2	0.0%	0.0%	0.0%	0.0%	0.0%	0.0%	0.0%	0.0%	0.0%	0.0%	0.0%	0.0%
H_2O	36.3%	31.4%	27.6%	22.2%	17.8%	15.7%	13.8%	11.3%	8.5%	5.0%	1.2%	0.0%
N_2	0.0%	0.1%	0.1%	0.1%	0.0%	0.0%	0.0%	0.0%	0.0%	0.0%	0.0%	0.0%
CO_2	24.0%	21.7%	19.7%	16.7%	13.9%	12.6%	11.3%	9.4%	7.4%	4.5%	1.0%	0.0%
CH_4	6.0%	10.0%	13.6%	19.4%	25.3%	28.0%	31.3%	35.2%	40.6%	47.4%	58.3%	92.6%
CO	7.3%	8.3%	9.1%	10.2%	11.0%	11.4%	11.6%	12.1%	12.4%	13.0%	12.9%	0.2%
C_2H_6												2.8%
Total	100.0%	100.0%	100.0%	100.0%	100.0%	100.0%	100.0%	100.0%	100.0%	100.0%	100.0%	99.7%

Table 16: Anode fuel stream composition at different steam-to-carbon ratios

Overall, the anode fuel stream composition is enriched with methane, while the steam content drops as steam-to-carbon ratio decreases. The elemental composition corresponding to individual steam-to-carbon ratios was calculated based on the anode fuel stream composition in Table 16 and is listed in Table 17.

S/C	3.0	2.0	1.5	1.0	0.7	0.6	0.5	0.4	0.3	0.2	0.1	0.001
C	13.4%	14.1%	14.7%	15.6%	16.3%	16.7%	17.0%	17.4%	17.9%	18.5%	19.1%	19.9%
H	53.7%	56.5%	58.9%	62.3%	65.3%	66.6%	68.0%	69.6%	71.6%	73.8%	76.6%	80.0%
O	32.9%	29.3%	26.4%	22.1%	18.4%	16.7%	15.0%	13.0%	10.5%	7.7%	4.2%	0.0%
Total	100.0%	100.0%	100.0%	100.0%	100.0%	100.0%	100.0%	100.0%	100.0%	100.0%	100.0%	100.0%

Table 17: Elemental composition of anode fuel stream at different steam-to-carbon ratios

A schematic of test set-up for pressurized carbon deposition experiment is shown below in Figure 23.

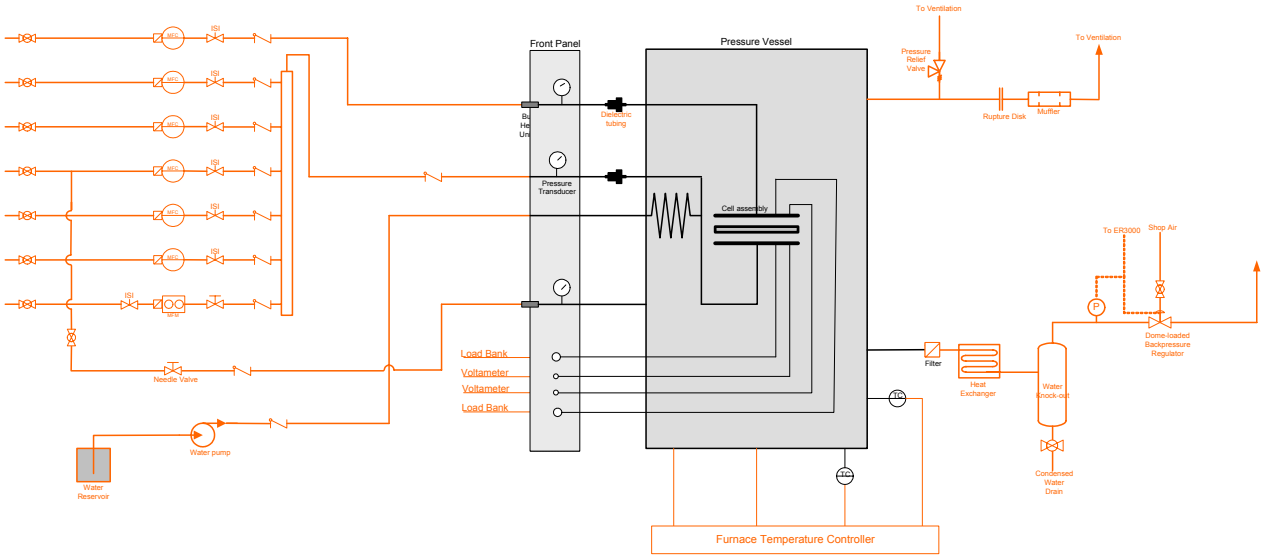

Figure 23: Schematic of test set-up for pressurized carbon deposition experiments

A single cell module was housed inside a cylindrical pressure vessel, equipped with an electrical furnace for heating up of the cell module. Programmable temperature controllers were employed for precise and programmed temperature control of the vessel. Mass flow controllers were used for precise and controlled flow rates of individual fuel gases. These individual gas flows were mixed and then introduced to the anode flow field. The anode fuel stream was preheated as it travels through the fuel preheating line in the vessel. A separate water line from the liquid water pump entered the vessel and steam was generated as it traveled through the coiled water preheating line before entering the anode fuel preheating line as shown in Figure 23. Radial seal-less single cell SOFC modules of 3-inch diameter were used for ambient pressure experiments while 4 3/8-inch radial seal-less single cell SOFC modules were used for pressurized (44.1 psig) experiments. With the radial seal-less cell module, excess fuel in the anode exhaust stream that had not been consumed at the anode was combusted along the circumference of the cell. This helped to maintain the overall cell temperature. For pressurized tests, a back pressure regulator was employed to pressurize the cell. For safety purposes, the pressure vessel was equipped with a pressure relief valve. The pressure relief valve opened up to prevent any excessive and accidental pressure build-up inside the vessel. The test set-up was interfaced with a digital data acquisition system that loged time stamped information such as individual gas flows, temperature, cell voltage and current. A pressure transducer was installed upstream of the fuel preheating line outside the furnace and pressure vessel and the pressure in the fuel line was monitored to ensure there is no flow blockage.

2.2.1.3 Test Results

2.2.1.3.1 Ambient Pressure Experiments

Altogether, 10 cells were assembled and tested for carbon deposition experiments at ambient pressure during this reporting period. Initial tests were used for verifying and troubleshooting the test setup, and for rough mapping of the carbon deposition regions. Later tests were used to pinpoint the carbon deposition regions.

Figure 24 shows cell voltage and upstream fuel line pressure plotted as a function of time for different anode fuel stream compositions. As specified above, the cell was first reduced and then conditioned at 457 mA/cm^2 for 20 hours. This conditioning procedure increased cell voltage from 0.617V to 0.670V. Following the cell conditioning, the anode fuel stream was transitioned to a steam-to-carbon ratio of 1.0, with fuel composition as specified in Table 16. In previous cell tests, stable cell performance on steam-to-carbon ratio of 1.5 (S/C 1.5) had been demonstrated several times and so it was considered safe to start at this condition to establish stable operation without carbon deposition after cell conditioning. The total anode fuel flow rate after the cell conditioning was controlled throughout the whole test period to maintain fuel utilization of 28.6% at current density of 286mA/cm^2 at an operating cell voltage above 0.7V.

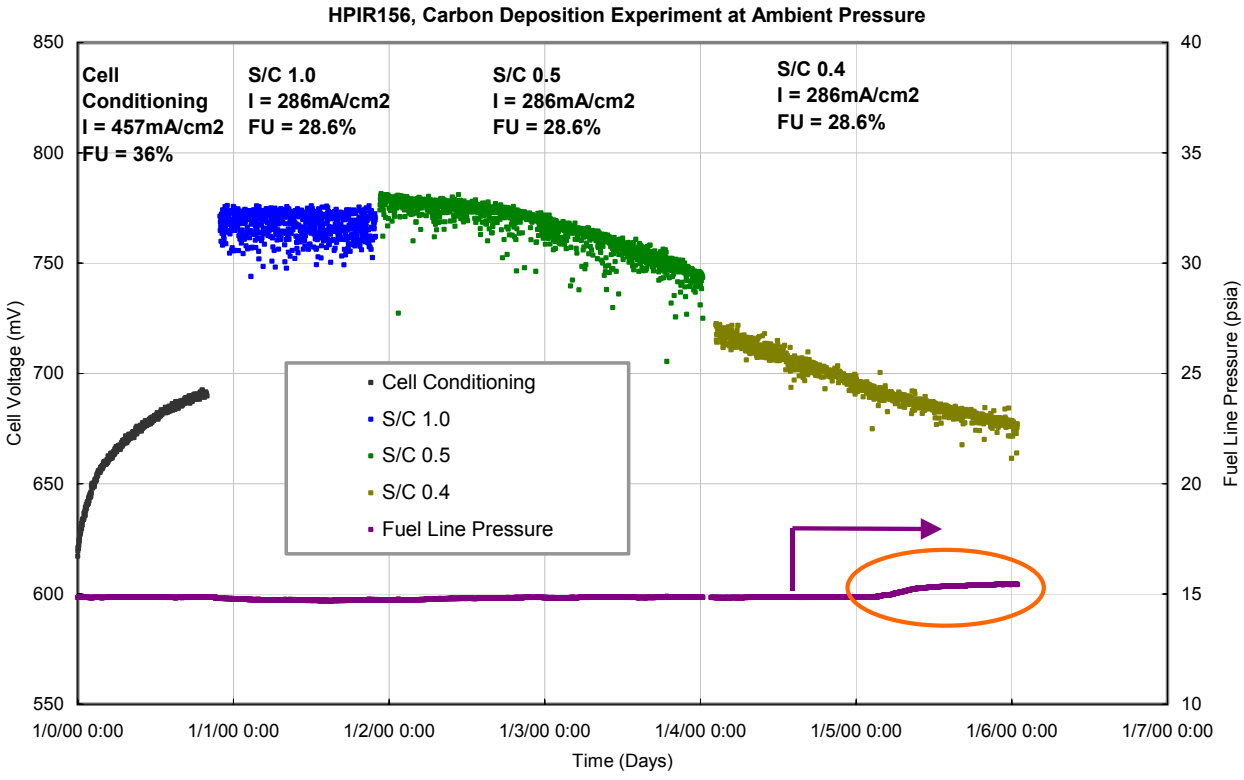

Figure 24: Carbon deposition experiment result at ambient pressure

As shown in Figure 24 the cell maintained stable cell voltage of 0.77 ± 0.015 V for 24 hours at anode fuel stream S/C of 1.0. Fluctuations in cell voltage was observed

generally on cells running on reformate fuel streams containing steam. These fluctuations were caused by fluctuations in the steam generation for the test. The degree of voltage fluctuation was experimentally observed to be higher as the anode fuel stream was enriched with steam.

After reaching 24 hours of cell operation on S/C 1.0 anode fuel stream, anode fuel stream was transitioned to S/C 0.5. At this condition the cell showed very slow and gradual voltage drop without increase in fuel line pressure, indicating carbon deposition on the cell. The cell voltage dropped from 0.777V to 0.769V over 24 hours (voltage drop rate 0.333mV/hr). The cell was subsequently operated for a second 24 hours duration on S/C 0.5 anode fuel stream. The cell voltage continued to drop gradually (from 0.769V to 0.743V) but at an increased rate of 1.08mV/hr. As the cell voltage drop rate measured was fairly low and the cell voltage remained above 0.7V, even after 48 hours of cell operation on S/C 0.5, it was decided to reduce the steam content further to S/C 0.4 for an extended period of time (another 48 hours) as shown in Figure 24. The cell voltage drop rate on S/C 0.4 anode fuel stream for 48 hours was measured to be approximately 0.90mV/hr and this rate was very close to the one measured on S/C 0.5 anode fuel stream. A slight increase in the fuel line pressure was observed (from 14.9 psia to 15.4 psia) while the cell was operated on S/C 0.4 anode fuel stream. The fuel line pressure rise was later found to be due to the clogging of the dry fuel line upstream of the steam mixing point due to carbon deposition. The amount of carbon left inside the fuel preheating line was measured and assuming that the carbon deposition inside the fuel preheating line occurred for 48 hours, it corresponded to less 2% of methane flow rate in S/C 0.5 anode fuel stream. As the fuel utilization level in this experiment was low (28.6%), methane consumed for carbon deposition in the fuel preheating line was considered to have very minimal effect on cell voltage drop observed on S/C 0.5 and 0.4 anode fuel stream.

The cell was cooled down after reaching 48 hours of operation on S/C 0.4 anode fuel stream and the cell assembly was removed from cell stand and the cell was tore open from the endplates to inspect for any changes in cell structure or to locate any carbon deposits that may have been formed over the anode flow field or the cell anode surface.

Figure 25 shows an image of cell anode after the conclusion of the ambient test described above. It appears that the anode is in a reduced state (gray color of metallic nickel) and no carbon species were visually found. The small black powder along the edge of anode cell pieces in Figure 25 is cathode material.

Figure 25: Image of cell anode taken out after carbon deposition experiment at ambient pressure

The cell anode was further inspected using SEM-EDX surface analysis techniques. Various points across the anode layer were inspected. Figure 26 shows a typical SEM-EDX spectrum obtained from the cell anode of Figure 25. A small C peak is present in the spectrum on both YSZ (left) and Ni (right) particles. Anode with visible carbon deposit is reported to yield a C peak that is comparable in size to the Zr peak. Considering the little C peak on SEM-EDX spectrum in Figure 26, the carbon deposition was considered to occur fairly slowly on both S/C 0.5 and 0.4 anode fuel streams and that slow carbon deposition rate resulted in low cell voltage drop rate as shown in Figure 24.

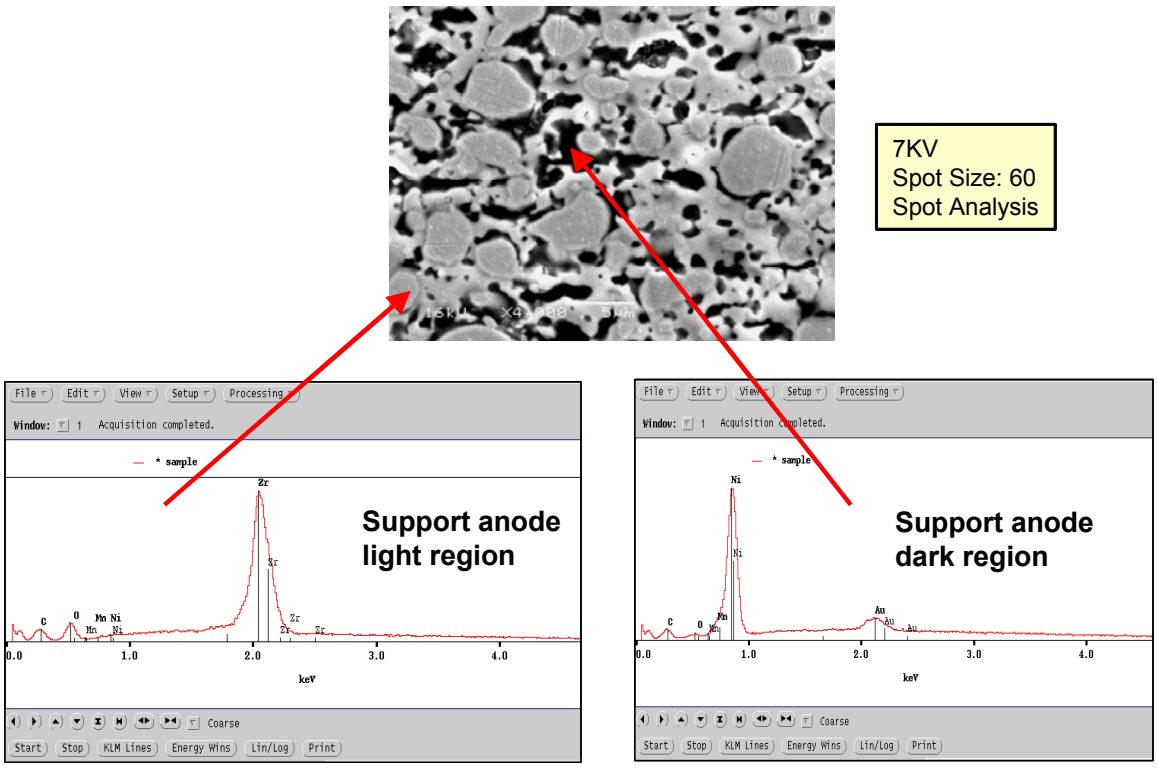

Figure 26: SEM-EDX spectrum taken from anode support layer after carbon deposition experiment at ambient pressure

Thermodynamic calculations predict that the carbon deposition boundary lies between S/C 0.6 and S/C 0.7 anode fuel stream composition of Table 16 at ambient pressure and 800°C. The results of the experiment (carbon deposition at S/C of 0.5 and 0.4) are consistent with the thermodynamic calculations.

2.2.1.3.2 Elevated Pressure (44.1 psig) Experiments

Two pressurized tests were conducted on 4-3/8 inch circular seal-less SOFC single-cell modules. The assembled cell went through cell reduction and cell conditioning before pressurization. The cell voltage and fuel line pressure data collected during this test is shown in Figure 27.

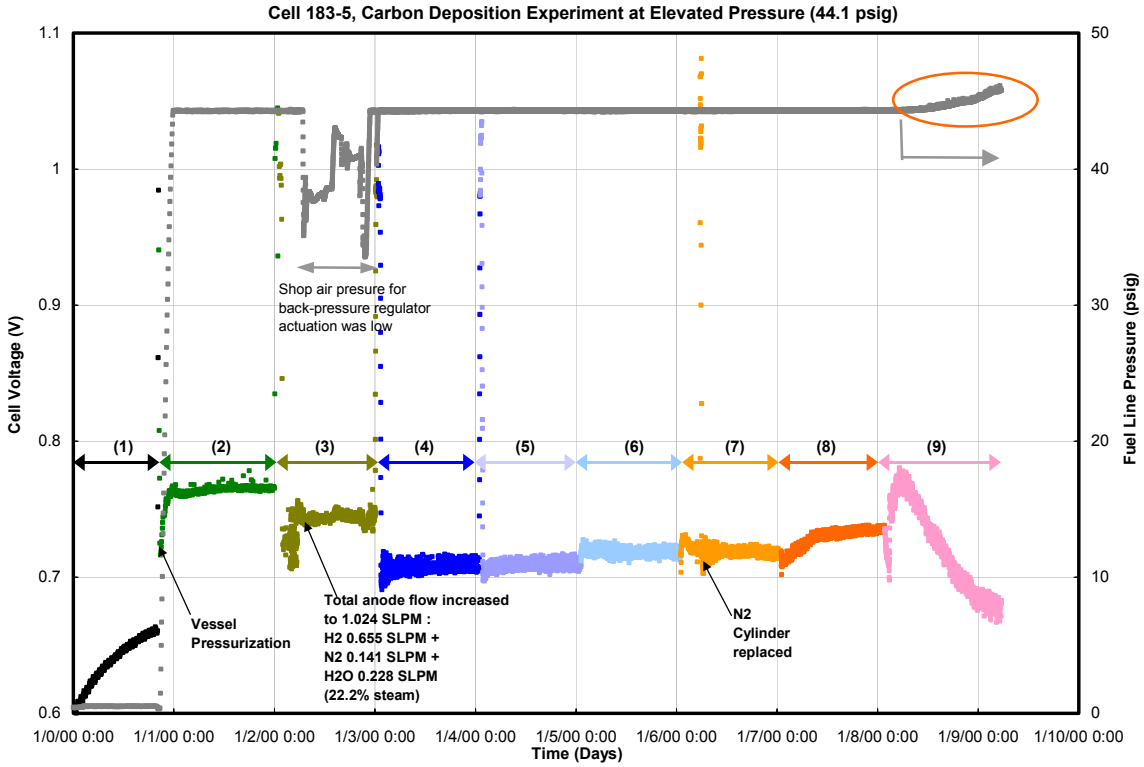

Figure 27: Carbon deposition experiment result at 44.1 psig pressure (numbers in parentheses refer to flow conditions detailed in Table 18)

Anode Fuel Streams employed in Carbon Deposition Test at Elevated Pressure	Current Density (mA/cm^2)	Fuel Utilization (%)	Carbon Deposition Predicted	
			Open Circuit	Under Load
(1) Cell Conditioning, H_2 0.64 SLPM + N_2 0.36 SLPM	370	29.4		
(2) H_2 0.51 SLPM + N_2 0.29 SLPM	286	28.6		
(3) H_2 0.51 SLPM + N_2 0.11 SLPM + H_2O 0.177 SLPM	286	28.6		
(4) S/C 2.0 + N_2 0.363 SLPM,	286	28.6	NO	NO
(5) S/C 1.0 + N_2 0.598 SLPM	286	28.6	NO	NO
(6) S/C 0.7 + N_2 0.672 SLPM	286	28.6	NO	NO
(7) S/C 0.5 + N_2 0.723 SLPM	286	28.6	YES	NO
(8) S/C 0.3 + N_2 0.777 SLPM	286	28.6	YES	NO
(9) (S/C 0.5)x2.2 + N_2 0.362 SLPM	286	13.0	YES	NO

Table 18: Details of flow conditions used in pressurized carbon deposition experiment (see Figure 27)

The vessel was pressurized while the cell was operating on a hydrogen/nitrogen fuel stream. The anode fuel flow rate was maintained at 28.6% fuel utilization at 286mA/cm^2 current density. Pressurization of the vessel from 0 psig to 44.1 psig raised cell voltage from 0.713V to 0.764V.

After 24 hours of stable cell operation at these conditions, steam injection was initiated to understand the effect of steam on cell performance and stability at pressurized conditions. Liquid water flow rate was controlled to achieve 22.2% steam content by replacing part of the nitrogen flow in the anode fuel stream. The 22.2% steam content

was the same as that of S/C 1.0 in Table 16 and considered the representative steam content. A fluctuation in cell voltage (±15mV) was observed for the same reasons discussed above. The total anode flow rate was subsequently increased to 1.024 SLPM without changing the mole percentage of hydrogen, nitrogen, and the steam in the anode fuel stream (64% H2, 13.8% N2 and 22.2% H2O). The flow rate was increased because at high pressures the linear velocity is decreased, making it difficult to achieve local flow uniformity and adequate velocity at the exit to prevent back diffusion. Subsequently, all testing was performed with an anode flow rate of 1.024 SLPM by adding nitrogen as needed, to maintain adequate linear velocity. The increase in total anode flow rate raised cell voltage by 0.015V (from 0.73V to 0.745V) through reduced fuel utilization (from 28.6% to 22%).

After 24 hours of stable cell operation with a wet (22.2% H_2O) hydrogen/nitrogen anode fuel stream, the anode fuel stream was transitioned to a S/C 2.0 reformate stream. The cell voltage remained stable at approximately 0.705V for 24 hours of operation and showed no measurable sign of cell voltage degradation. Cell operation was continued by transitioning the anode fuel stream to lower S/C ratios (S/C 1.0, S/C 0.7, S/C 0.5 and S/C 0.3), as shown in Figure 27, for 24 hours each and after confirming stable cell operation at each S/C setting. The cell logged a total of 120 hours of operation.

Followed by the stable cell operation on S/C 0.3 reformate stream, the anode fuel stream was transitioned to S/C 0.5 reformate stream with reduced nitrogen flow rate. To compensate for the reduced nitrogen flow, but maintaining a total anode flow rate of 1.024 SLPM, the S/C 0.5 reformate stream flow rate was raised by 120%, which resulted in a lowered fuel utilization from 28.6% to 13.0%. It should be noted that the reduction of nitrogen flow rate and increase in S/C 0.5 reformate stream flow rate increased the partial pressure of individual reactant gases in the reformate stream. The initial cell voltage measured with S/C 0.5 reformate stream was higher (0.773V) than the preceding S/C 0.5 reformate stream test (0.717V). This higher cell voltage was considered to result from the increased reformate stream flow rate (by 120% compared to the preceding one) and the resultant low fuel utilization (13.0% vs 28.6%).

Once the cell voltage reached 0.773V, then it started to drop at the rate of approximately 4.1mV/hr, indicating carbon deposition. The cell voltage drop was accompanied by a rise in fuel line pressure. The fuel line pressure rise was moderate (less than 2 psi) and was not considered high enough to substantially impact anode flow. Cell operation was terminated under a controlled environment after the cell voltage dropped by approximately 0.1V. The cell module was cooled down under a controlled environment to conserve any carbon deposits that may have been formed.

No carbon deposits were found in the fuel preheating line upstream of the cell anode. Therefore, it is inferred that the gradual rise in fuel line pressure resulted from the accumulation of carbon deposits in the anode flow field, as seen in the figure.

SEM-EDX analysis was conducted on the cell. This revealed a morphology of carbon deposit over the anode surface that was found to be bulky carbon fibers and aggregated spherical carbon, as shown in Figure 28.

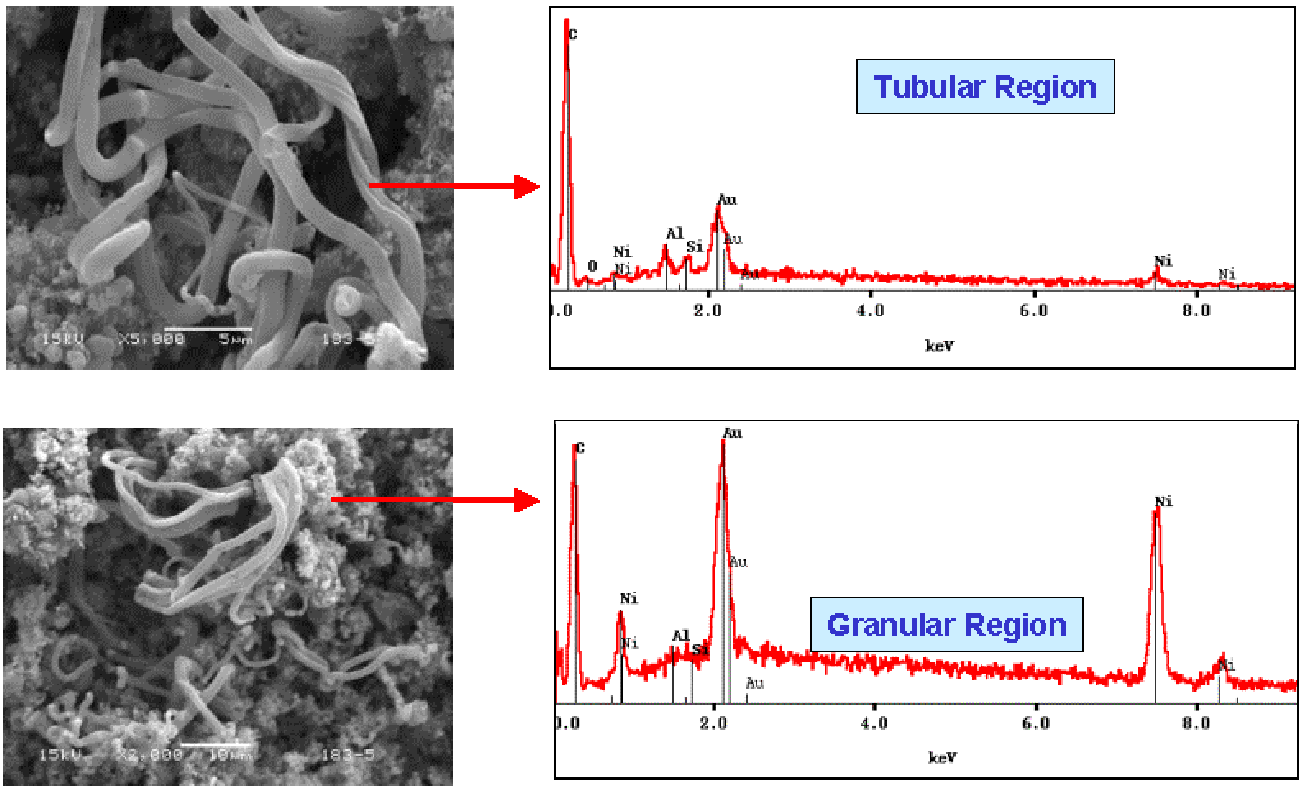

Figure 28: SEM image of carbon deposits over anode surface

The profile of carbon deposits across the anode layer was further investigated to determine whether carbon deposition occurred inside the anode layer. Figure 29 shows an optical microscopic image of the test cell cross-section in the regions where carbon deposits were observed at the anode surface. Dark black spots were found on certain areas in the active (electrochemical) anode layer. There were very few signs of carbon deposition in the support anode layer.

The carbon deposit profile was also checked at the electrolyte layer, active anode layer, and four other locations in the support anode layer. Figure 30 shows the location and the SEM-EDX spectra results. The C peaks in Figure 30 increase as the location moves toward the electrolyte layer. The active anode layer has the highest C peak. No noticeable C peak was found on the electrolyte layer. This observation does not support the general understanding that the anode inner layer is more enriched with H_2O and less enriched with methane compared to the anode outer layer. It is probable that carbon deposits closer to the anode/gas interface might have been removed through reaction with hydrogen during the cool down period of the test since low hydrogen flow was bled into the nitrogen stream during this period.

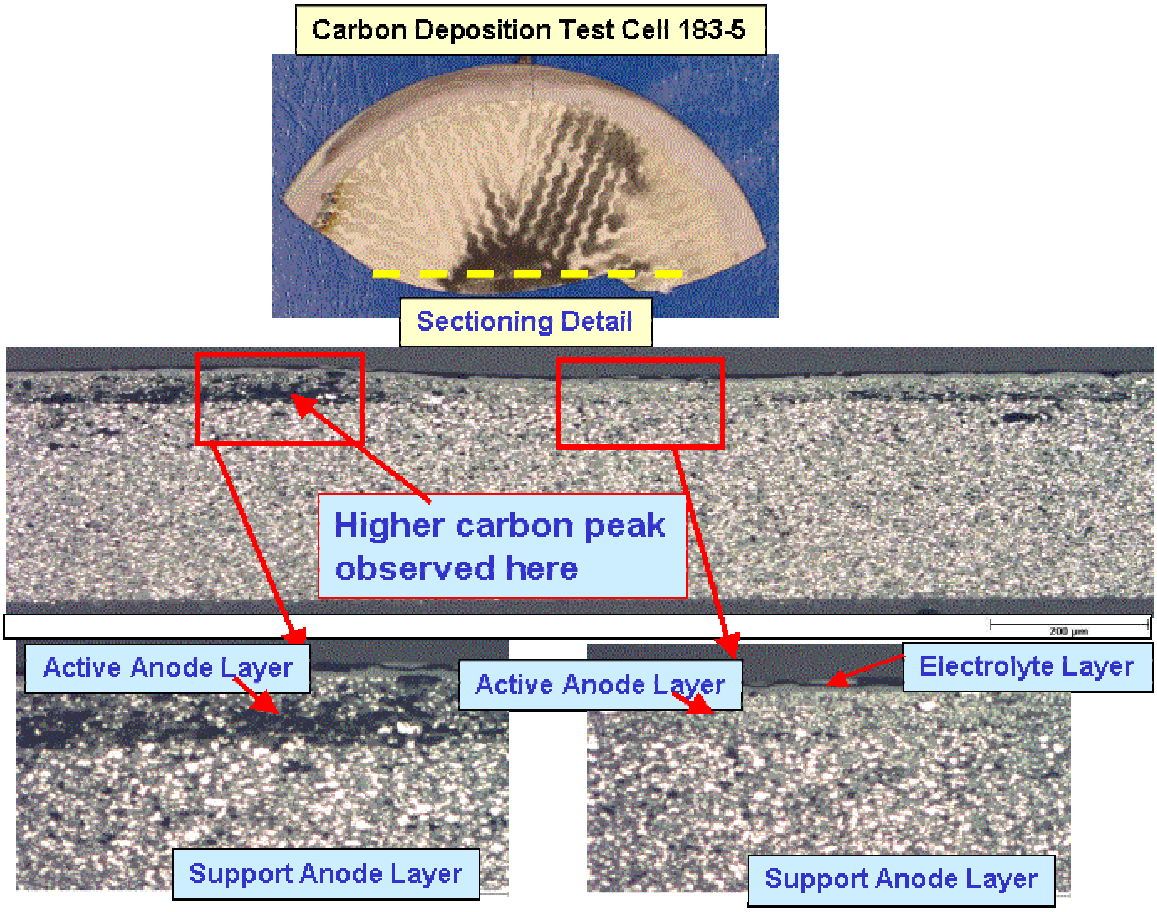

Figure 29: Optical microscopic image of test cell cross-section

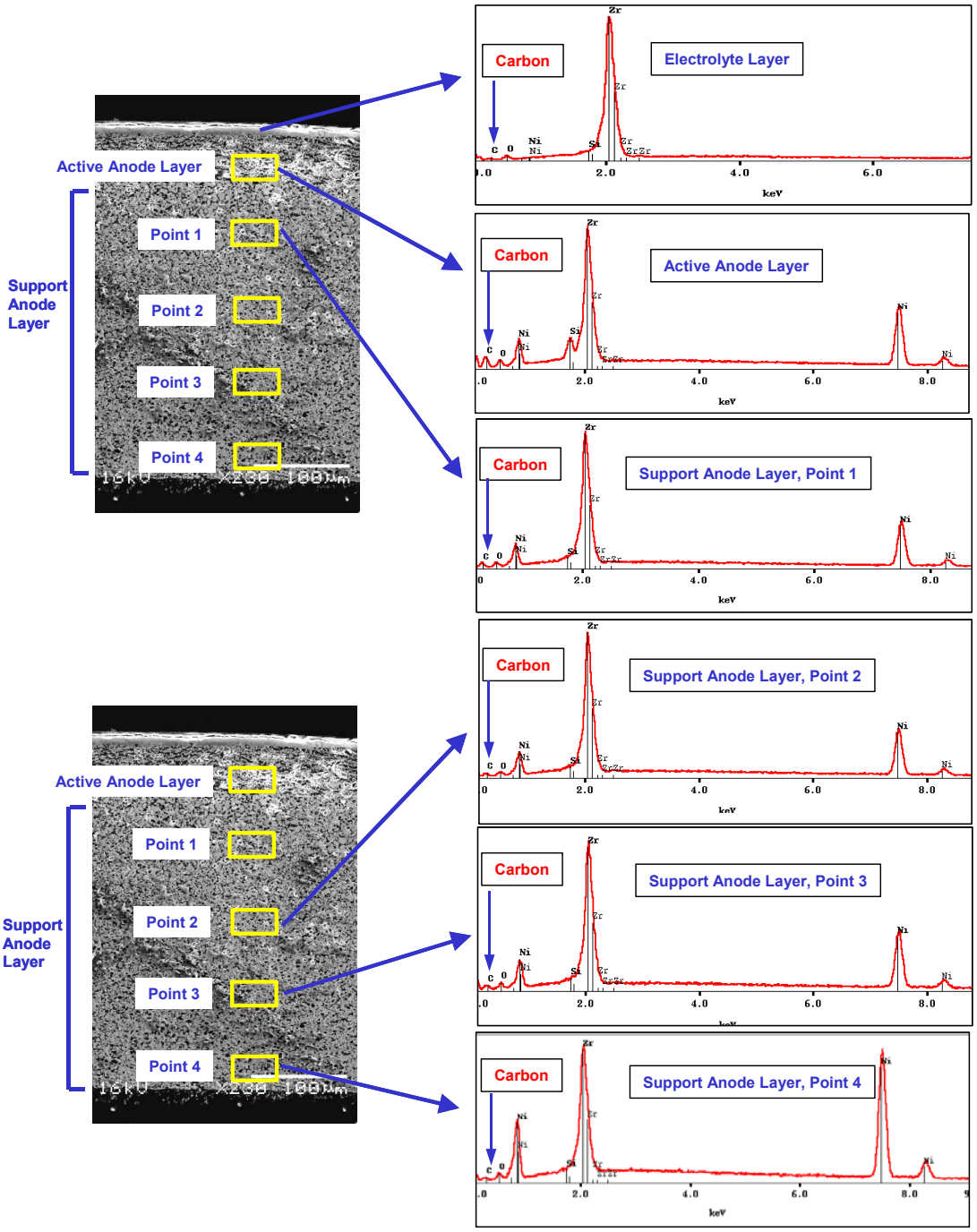

Figure 30: SEM-EDX spectrum across test cell cross-section

2.2.1.4 Discussions and General Conclusions

Along with the ambient and pressurized carbon deposition experiments as shown in Figure 24 and Figure 27, respectively, thermodynamic calculations were performed to understand the operating conditions that are likely to promote carbon deposition in an operating cell. Calculations for ambient pressure operation indicate that S/C 1.0 anode

fuel stream in Figure 24 does not deposit carbon under open circuit operating conditions (i.e. with no electric load drawn from the cell) while S/C 0.5 does deposit carbon. When oxygen transfer via current generation from the cell is accounted for, S/C 0.5 anode fuel stream is not predicted to deposit carbon.

Thermodynamic calculations at conditions employed in Figure 27 (elevated pressure) predicts that carbon boundary lies between "(6) S/C 0.7 + N_2 0.672 SLPM" and "(7) S/C 0.5 + N_2 0.723 SLPM" anode fuel streams. Current generation on "(7) S/C 0.5 + N2 0.723 SLPM" anode fuel stream at fuel utilization of 28.6% was shown to add enough oxygen so that no carbon deposition is predicted at the anode outlet region. In Figure 27, cell voltage drop was clearly observed with "(9) (S/C 0.5)x2.2 + N2 0.362 SLPM" anode fuel stream which is also predicted to deposit carbon under open circuit.

In general, the experimental observation of carbon deposition was in line with thermodynamic calculations at open circuit conditions. The higher the steam-to-carbon ratio in anode fuel stream of Table 16 or the higher the O content in C/H/O elemental composition in anode fuel stream of Table 17, the less likely carbon deposition would occur. The experimental results show that cell operation on anode fuel of S/C 1.0 reformate stream (both ambient and pressurized) was stable without any sign of cell voltage drop. This observation suggests that anode fuel compositions corresponding to S/C 1.0 or higher are in a safe operating zone.

Thermodynamically, carbon deposition is favored at pressurized condition. For example, the anode fuel stream composition of S/C 0.7 in Table 16 is predicted to deposit carbon at 3 atm (29.4 psig), but not at 2 atm (14.7 psig). However, its pressure dependence is considered to be very weak and, therefore, the carbon boundary in elemental C/H/O diagram of Figure 1 may not be moved significantly with pressurization. In a working cell, kinetic parameters (such as mass transfer, rate constants, etc) also play important roles along with thermodynamic driving force toward carbon deposition. All these factors are reflected in experimental observations and the contribution of individual factors would be gained more clearly through extensive work over wide ranges of experimental conditions.

2.2.2 Life Test

2.2.2.1 Task Objectives

The objective of this task is to determine the impact of pressurized operation on the The objective of this task is to determine the impact of pressurized operation on the SOFC performance stability. Prior to this task, most of the SOFC development and evaluation was focused on ambient conditions. No long-term data was available on planar SOFC's operated at elevated pressures. The goal of this task is to characterize the SOFC performance stability under pressurized operation and to compare it to that of ambient pressure operation.

2.2.2.2 General Approaches

In the early stages of this program, due to limitations in available test stands, SOFC performance had been evaluated at 2 atm with 3-inch cells. The preliminary data

indicated that SOFC performance appeared to decay faster than that under ambient conditions. In this reporting period, several long-term tests were completed. Most of the tests used 4 3/8-inch circular cells with radial sealess design and were conducted at nominal 800°C with 64%H_2/36%N_2 as fuel and air as oxidant. These cells consisted of YSZ electrolyte separating Ni/YSZ anode and LSM/YSZ cathode. Commercially available ferritic alloy was used as interconnect. To reduce interference of fuel utilization, these tests were conducted under moderate fuel utilization (~40%). During tests, the cells were operated under a given current density and pressure, and the cell voltage was monitored over the testing period to evaluate its performance. Cell area specific resistance (ASR) was also estimated from the cell open circuit voltage, operating voltage, and current density. In some tests, AC impedance was also taken before and after the test to evaluate the change in cell impedance. Post test analysis was conducted to characterize the cell microstructure, oxide scale on metallic interconnect, and chromium contamination to electrodes.

2.2.2.3 Fuel Cell Test Results

Figure 31 shows the performance (cell voltage and ASR) of Cell 122 as a function of time under test conditions. After cell reduction and initial polarization, the cell was held at 0.435A/cm^2 and 1atm (ambient pressure). The cell performance continued rising in the first 200 hours and it appeared to be steady between 300-500 hours. The initial performance increase with time is typical for these cells. However, it appears to take longer for the performance to stabilize or start to decay. This process has not been well understood and it is often referred to as “conditioning” of the cell, especially the electrodes. Since the “conditioning” process was long, a higher current density (0.473 vs 0.435 A/cm^2) was used to accelerate the process. However, the cell performance started to decay rapidly, even when the cell returned to the original current density (0.435 A/cm^2).

Nevertheless, the cell module was pressurized to 4 atm and held at 0.435 A/cm^2 for further testing. Again, the cell decayed and the degradation rate appeared to be much faster (voltage loss of ~170 mV within 20 hours) than that at 0.435 A/cm^2 and ambient pressure. Afterward, the cell performance could not be sustained at a lower current density (0.323 A/cm^2). At this point, the cell test was terminated. It seemed that the cell was damaged during the current transition period even though the exact causes remained unclear.

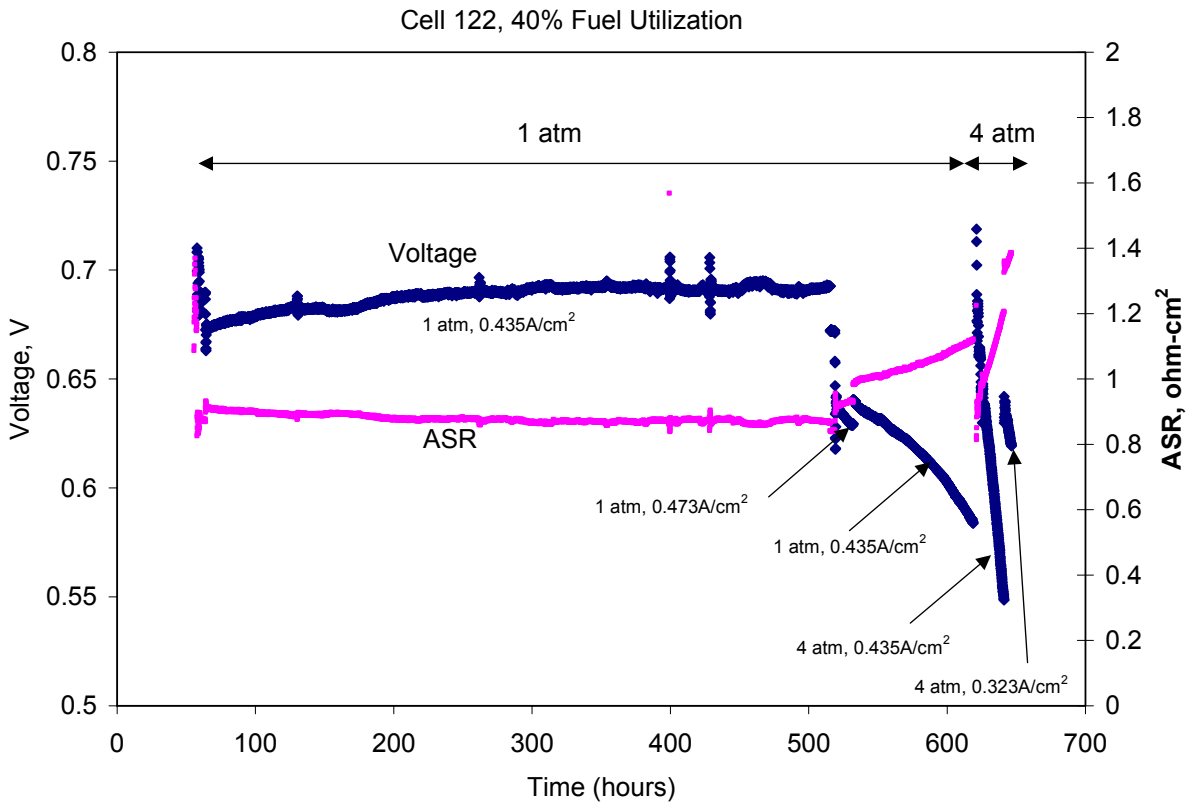

Figure 31: Performance of cell 122 at 800°C with 64% hydrogen balance nitrogen

In parallel to Cell 122, Cell 110 was also tested with the same objective. Figure 32 shows the performance with time of Cell 110. Similar to the Cell 122, the performance of Cell 110 improved over time in the first 640 hours, showing the cell voltage increase and ASR decrease under a fixed current density of 0.3A/cm^2. After approximately 650 hours, the cell was pressurized to 4 atm and held at current density of 0.379A/cm^2 for about 100 hours before the furnace malfunctioned. The furnace cooled down unexpectedly while the electronic load continued to draw current from the cell, which damaged the cell. In the approximately 100 hours testing period under 4 atm, the cell voltage appeared steady or slightly decreased in comparison to that observed at ambient pressure (Figure 33).

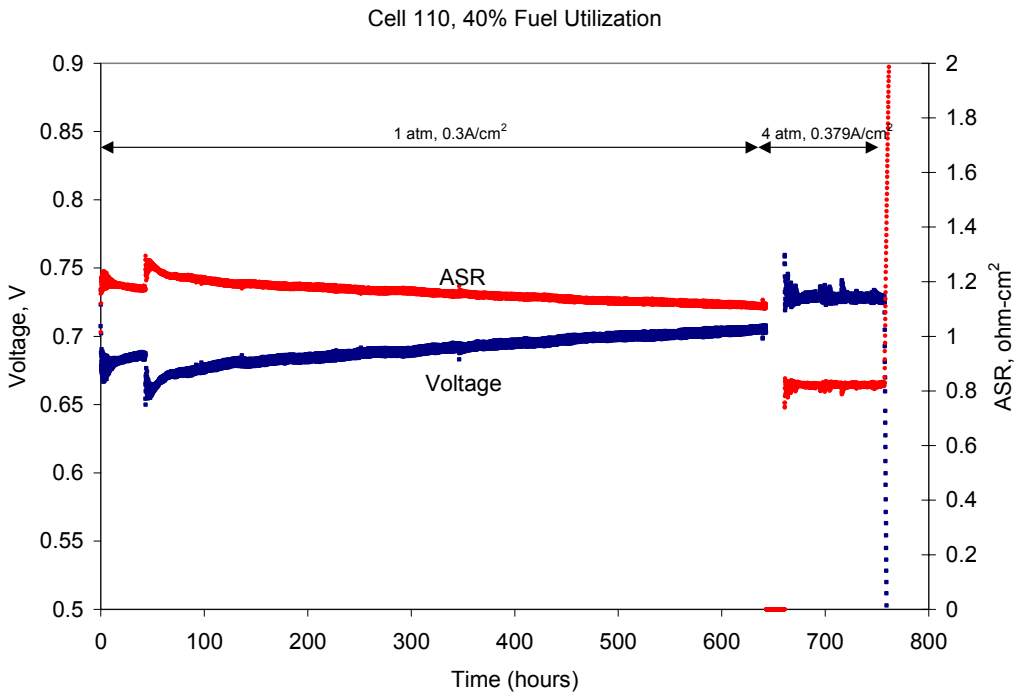

Figure 32: Performance of cell 110 at 800°C

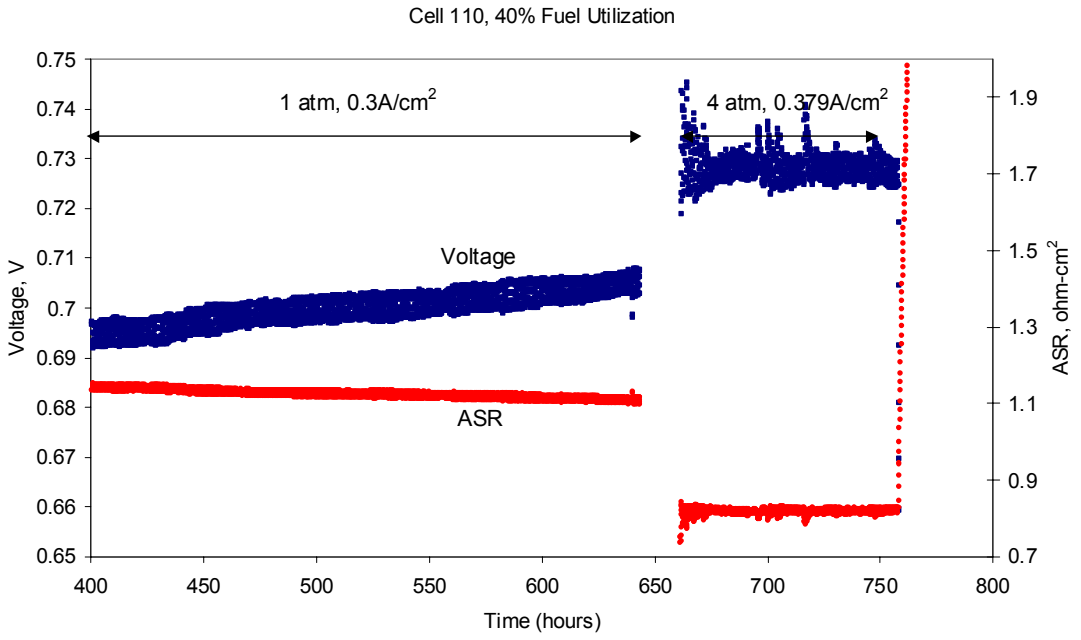

Figure 33: Performance data of cell 110 showing the transit between ambient pressure and pressurized conditions

Since the module performance increased with time in the initial testing period and this conditioning process under ambient pressure was relatively slow as indicated in Cell 110 and Cell 122 tests, a test plan was devised to obtain the performance stability trend under the pressurized conditions first and then switch to ambient conditions. Figure 34 shows the test history of Cell 104. It starts with a 4 atm hold, followed by several steps: at 1 atm, 4 atm, 3 atm, 1 atm and then back at 4 atm. The total duration of this test is more than 1000 hours. In the late stage of this test (from ~900 hours), the pressure fluctuated as much as 5 psi due to a malfunction of the back pressure controller.

During the whole testing period, the voltage appeared somewhat noisy. Despite this noise, the data clearly shows that pressure had a significant impact to the cell performance stability. Cell performance decayed under pressurized conditions in comparison to cell performance improvement (or "conditioning") at 1 atm in the testing period. Close examination of the test data and conditions indicated some of voltage fluctuation arose from the temperature fluctuation of the furnace. The error introduced by the temperature fluctuation was corrected with a transfer function of voltage and temperature obtained in the temperature range between 790 and 815°C. The temperature adjusted data is shown in Figure 35.

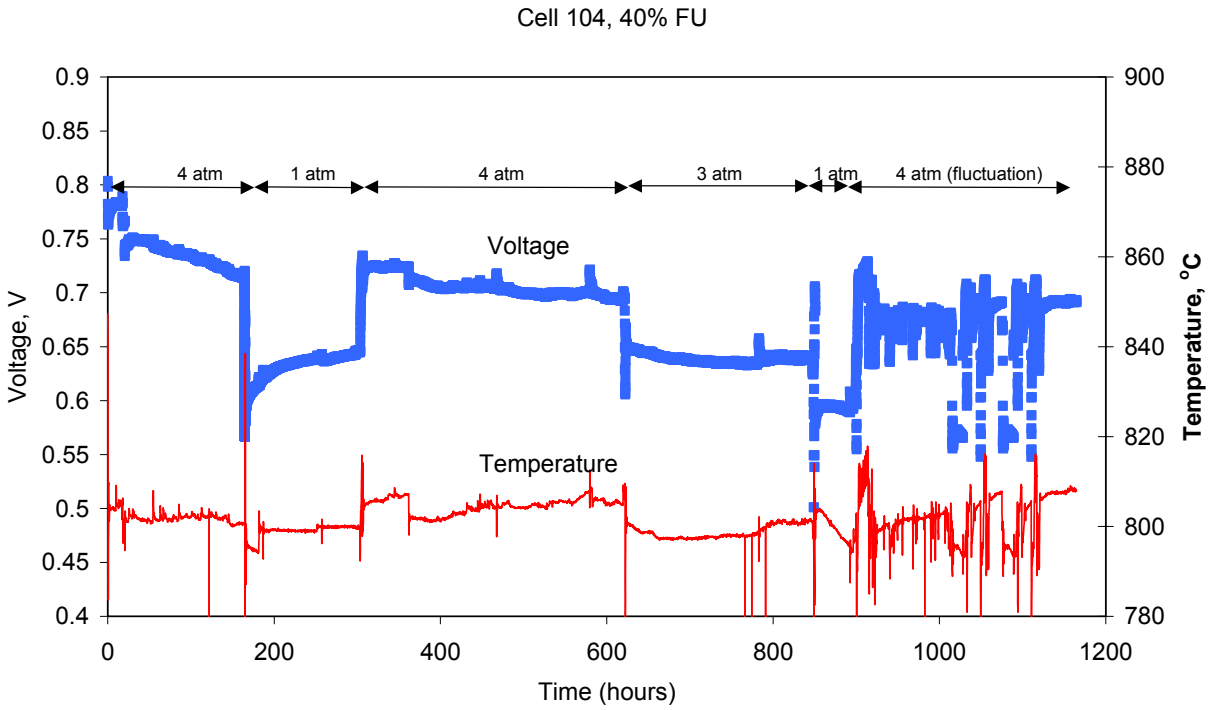

Figure 34: Testing history of cell 104 showing performance and temperature fluctuation

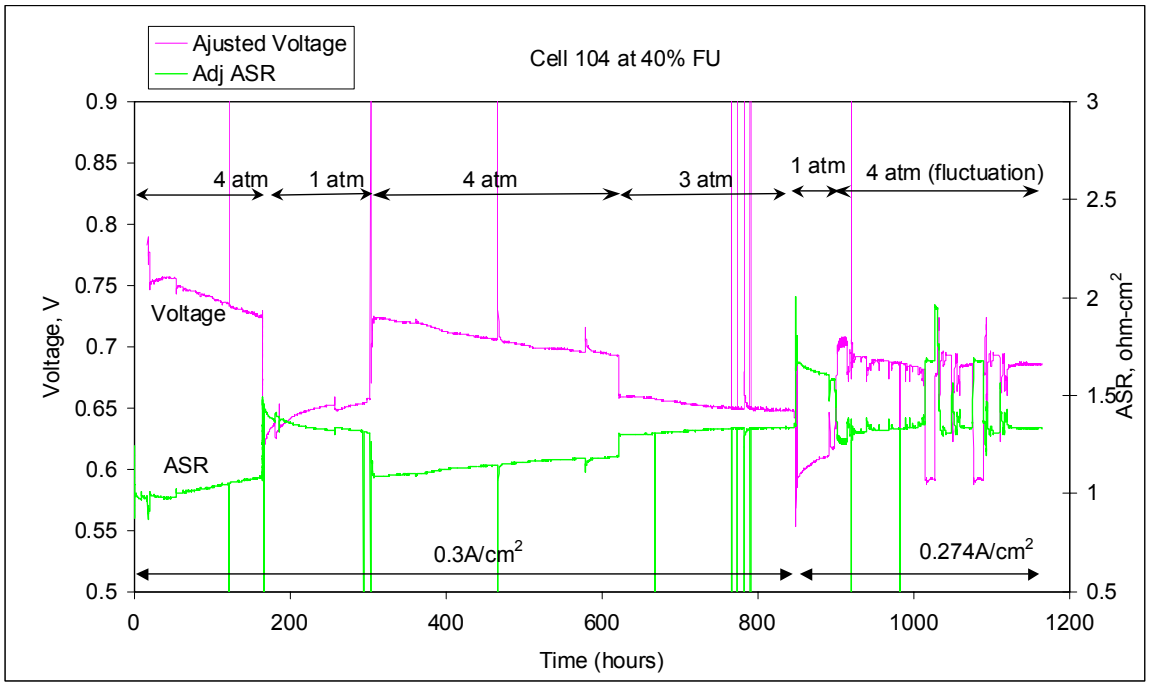

Figure 35: Performance of cell 104 after correction of temperature effect

As shown in Figure 35, the cell voltage decayed under pressurized conditions while the cell performance increased with time once it was switched back to ambient pressure. These results clearly demonstrate the pressure impact to the cell performance stability with time. Based on the data shown in Figure 35, the cell ASR (which includes both ohmic and non-ohmic losses) increased by ~350 mohm-cm^2 after being tested for about 1165 hours.

The AC impedance was also measured on Cell 104 under open circuit conditions at ambient pressure before and after the test. The impedance data (Figure 36) indicates that ohmic resistance of the module increased by ~182 mohm-cm^2 (from ~274 mohm-cm^2 at the beginning of the test to ~456 mohm-cm^2 at the end of the test after 1165 hours). This ohmic resistance increase is about half of the total ASR increase (~350 mohm-cm^2) observed in the performance evaluation.

The impedance analysis also shows that the electrode polarization increases. While the electrode polarization can be estimated from the impedance analysis in principle, the data shown in Figure 36 can only be used as reference because it represents the conditions under open circuit voltage (OCV) at ambient pressure. Due to instrument limitations, AC impedance could not be carried out with current load.

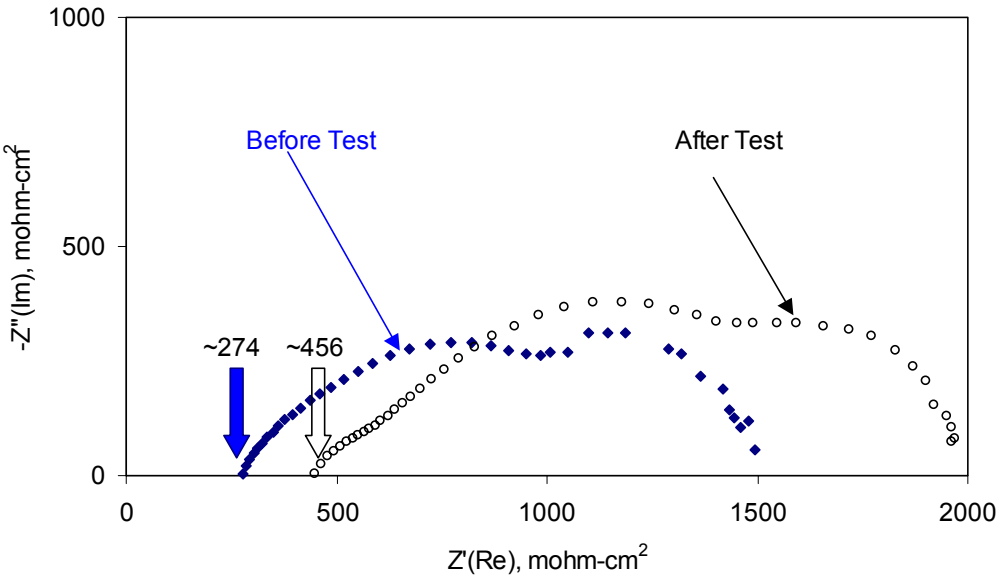

Figure 36: AC impedance taken at 800°C under OCV before and after test

2.2.2.4 Post Test Analysis

Post-test analysis on Cell 104 (Figure 37) did not reveal micro structural anomalies in the cell cathode, electrolyte, and anode in comparison to the cells tested under ambient pressure. The oxide scale was about 2 micron thick, for both the cathode and anode side interconnect (Figure 38). The oxide thickness is similar to those cells tested at ambient pressure for a comparable duration. Silicon-containing material was also detected under the chromium-rich oxide scale. The silicon is believed to be an impurity in the interconnect metal.

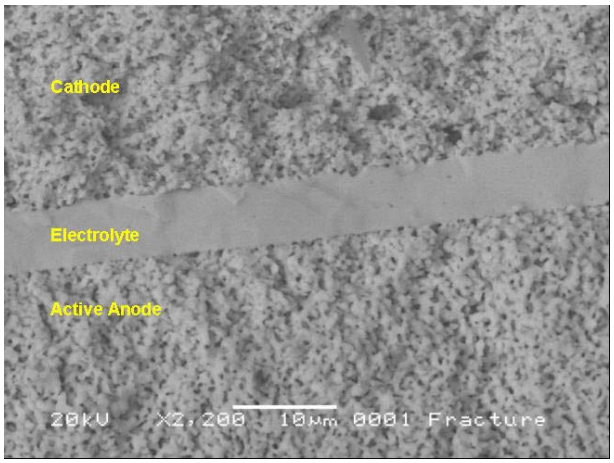

Figure 37: Fracture surface of cell 104 after being tested for more than 1000 hours under pressure

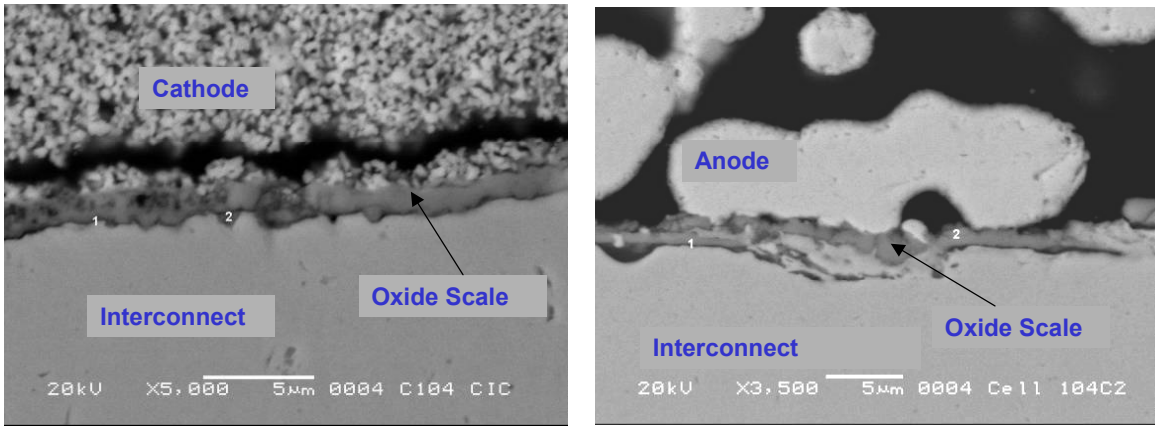

Figure 38: Cross-sections of cell 104 showing oxide growth at both cathode and anode side interconnect

Using an EDX line scan, Chromium was detected between the LSM/YSZ cathode and the metallic interconnect. A slight chromium pile up at the electrolyte/cathode interface was also noticed in the analysis. It appears that the chromium species of metallic interconnect transported and interacted with the cathode materials.

Detailed composition analysis was also conducted on Cell RJ019, which was tested for about 1000 hours. Most of the test time of this cell was at 2 atm pressure. Electron probe micro-analysis (EPMA) was performed in the areas under the interconnect fin (direct current path) as well as the areas open to the gas channel. There are several interesting observations from this data:

- The local chromium pileup at the cathode/electrolyte is clearly seen. In the center and middle portions of the cells, ~1.5-1.6% Cr is observed at the cathode/electrolyte interface. Lower Cr (~0.5%) is present in the edge areas of the cell.
- Chromium presence in a majority of the cathode is low except at the two interface areas.
- Higher chromium (3-5%) is present in the cathode

The profile looks similar to that under the fin area with two exceptions:

- Chromium presence is lower in the gas channel area compared to the area under fin
- At the cathode/electrolyte interfaces, Cr is less than 0.7% and there is little difference from cell center to edge

It is reasonable to believe that the local current densities are higher under the fin areas than the neighboring areas under the gas channels. Since both fuel and air flow is radial from the center to the edge, current density at the center is likely to be higher than that at the edge because of the fuel concentration difference (assuming the temperature is similar). In conjunction with the chromium profile observation, it seems that the Cr

transport and interaction with cathode materials may be current related. The higher current density may favor Cr deposition.

2.2.2.5 Hypothesis on Degradation Mechanisms

Major potential causes to cell performance decay include oxidation of metal interconnect, Cr poisoning to electrodes, interface resistance increase, electrode microstructure changes, back diffusion/leakage, and/or electrode conditioning process.

For oxide growth, the parabolic kinetics gives

$$x^2 = k_p t$$

$$or$$

$$x = k_p^{0.5} t^{0.5}$$

where x is the thickness of the oxide scale, k_p is the parabolic rate constant (thickness based) and t is the oxidation time.

For Cr-containing ferritic alloys, the parabolic rate constant depends on the self-diffusion coefficient of Cr and self-diffusion of oxygen. It has been found that the Cr outward diffusion to the oxide scale surface dominates the oxidation kinetics. At a given elevated temperature, the oxygen partial pressure, Po_2 dependence of the parabolic rate constant k_p can be estimated with diffusion coefficient of Cr ion in Cr_2O_3

$$k_p \propto D_{Cr} \propto P_{O_2}^{3/16}$$

Thus, the oxide growth thickness based on parabolic kinetics can be estimated as

$$x \propto P_{O_2}^{3/32} t^{0.5}$$

Assuming this relationship is valid for the testing conditions, the thickness of oxide scale in oxidizing environment is expected to increase by approximately 7%, 11%, 14% when pressure increases from 1 to 2, 3, and 4 atm, respectively. As indicated in Figure 38, the oxide scale was about 2 micron after 1165-hour test, which is not much different from those samples tested for similar duration under ambient pressure. It is inconclusive on whether or not the oxide scale grows faster under higher pressures due to the following reasons:

- The resolution is low for moderate growth rate increase under pressures tested, based on parabolic kinetics and the thickness measurements
- The thickness of the oxide scale observed is not representative since the oxide layer can also react with oxygen and water vapor to form vapor species

Another possible degradation mechanism is the chromium poisoning of the cathode, as observed in post-test analysis. This could be electrochemical reaction driven and/or chemical reaction driven. Considering chromium oxide and vapor formation reactions:

- $2Cr\ (s) + 3/2O_2\ (g) = Cr_2O_3\ (s)$ (1)
- $Cr_2O_3\ (s) + 3/2O_2\ (g) = 2CrO3\ (g)$ (2) or

- Cr_2O_3 (s) + 3/2O_2 (g) +2H_2O(g) =2$CrO_2(OH)_2$(g) (3)

Reaction 1 describes the chromium oxide scale formation on Cr-containing ferritic alloys, which will increase the oxide scale thickness as described with parabolic oxidation kinetics. Reaction 2 and 3 describe the possible chromium vapor formation, which could poison the cathode. Under the test conditions, the most possible chromium species may be chromium oxyhydroxide from reaction 3 because of the inevitable presence of H_2O impurity in the air used. The exact mechanism of the chromium contamination through chromium vapor species is unclear at this stage. However, higher operating pressure favors higher chromium-species pressures. Thus, the driving force for chromium vapor species diffusion and subsequent reaction with active cathode materials will be higher under higher pressure.

Other possible degradation mechanisms could also come in play, such as interface resistance increase, electrode microstructure changes, back diffusion/leakage, and/or electrode conditioning process. Exploration of those reaction mechanisms is beyond the scope of this task.

2.2.2.6 Summary

In summary, a number of SOFC module tests have been completed to evaluate the pressure impact to performance stability. The results clearly demonstrate that the operating pressure accelerates the performance degradation. The potential causes to the performance decay include oxidation of the metal interconnect, chromium poisoning to electrodes, interface resistance increase, electrode microstructure changes, back diffusion/leakage, and/or electrode conditioning process. The dominant degradation mechanisms remain unclear. However, current density appears to have an enhanced effect on chromium interaction with cathode material. Both interconnect oxidation and Cr transport to cathode were evident based on post-test analysis. To reduce the degradation related to metallic interconnect, interconnect materials have to be improved or protected with a coating. Future work is needed to understand the degradation mechanisms and the impact of pressure on the electrode conditioning processes.

Conclusion

During the phase 1 system design and technical barrier resolution task the following activities have been accomplished

- The conceptual design of a SOFC-hybrid system estimated to have 65% efficiency, a first cost of approximately $646/kW and a cost of electricity of 8.4 cents/kW-hr. A control strategy and conceptual control design have been developed for this system.
- Tests to explore the impact of pressure on the performance on SOFC's.
- High temperature heat exchanger design, fabrication, and testing as well as oxidation testing to support heat exchanger life analysis.

While technical challenges remain in the area of pressurized operation of SOFC's, the feasibility of highly efficient hybrid systems integrating a planar SOFC's and a micro-turbine have been shown.

References

1. "Scale-up Study of 5 KW SECA Modules to a 250 kW System", TIAX LLC Final Report to DOE/NETL, Reference: 74313, June 10, 2002.
2. K. Sasaki and Y. Teraoka, Journal of the Electrochemical Society, 150 (7), A885, 2003